

# Tropical Cirrus in Global Storm-Resolving Models. Part I: Role of Deep Convection

Jacqueline M Nugent<sup>1</sup>, Samantha M Turbeville<sup>1</sup>, Christopher S. Bretherton<sup>1</sup>, Peter N. Blossey<sup>1</sup>, and Thomas P Ackerman<sup>1</sup>

<sup>1</sup>University of Washington

November 23, 2022

## Abstract

Pervasive cirrus clouds in the upper troposphere and tropical tropopause layer (TTL) influence the climate by altering the top-of-atmosphere radiation balance and stratospheric water vapor budget. These cirrus are often associated with deep convection, which global climate models must parameterize and struggle to accurately simulate. By comparing high-resolution global storm-resolving models from the Dynamics of the Atmospheric general circulation Modeled On Non-hydrostatic Domains (DYAMOND) intercomparison that explicitly simulate deep convection to satellite observations, we assess how well these models simulate deep convection, convectively generated cirrus, and deep convective injection of water into the TTL over representative tropical land and ocean regions. The DYAMOND models simulate deep convective precipitation, organization, and cloud structure fairly well over land and ocean regions, but with clear intermodel differences. All models produce frequent overshooting convection whose strongest updrafts humidify the TTL and are its main source of frozen water. Inter-model differences in cloud properties and convective injection exceed differences between land and ocean regions in each model. We argue that global storm-resolving models can better represent tropical cirrus and deep convection in present and future climates than coarser-resolution climate models. To realize this potential, they must use available observations to perfect their ice microphysics and dynamical flow solvers.

**Tropical Cirrus in Global Storm-Resolving Models.  
Part I: Role of Deep Convection**

**J. M. Nugent<sup>1</sup>, S. M. Turbeville<sup>1</sup>, C. S. Bretherton<sup>1,2</sup>, P. N. Blossey<sup>1</sup>, and  
T. P. Ackerman<sup>1,3</sup>**

<sup>5</sup>Department of Atmospheric Sciences, University of Washington, Seattle, WA

<sup>6</sup>Vulcan, Inc., Seattle, WA

<sup>7</sup>Joint Institute for the Study of the Atmosphere and Ocean, University of Washington, Seattle, WA

**Key Points:**

- Characteristics of tropical cirrus over land and ocean in nine global storm-resolving models (GSRMs) scatter around observational ranges
- Most GSRMs reasonably simulate convective organization and rainfall, but with diverse vertical cloud structure through the upper troposphere
- Deep convection supplies most water to the tropical tropopause layer, with inter-model differences due to updraft speeds and microphysics

15 **Abstract**

16 Pervasive cirrus clouds in the upper troposphere and tropical tropopause layer (TTL)  
 17 influence the climate by altering the top-of-atmosphere radiation balance and stratospheric  
 18 water vapor budget. These cirrus are often associated with deep convection, which global  
 19 climate models must parameterize and struggle to accurately simulate. By comparing  
 20 high-resolution global storm-resolving models from the Dynamics of the Atmospheric gen-  
 21 eral circulation Modeled On Non-hydrostatic Domains (DYAMOND) intercomparison  
 22 that explicitly simulate deep convection to satellite observations, we assess how well these  
 23 models simulate deep convection, convectively generated cirrus, and deep convective in-  
 24 jection of water into the TTL over representative tropical land and ocean regions. The  
 25 DYAMOND models simulate deep convective precipitation, organization, and cloud struc-  
 26 ture fairly well over land and ocean regions, but with clear intermodel differences. All  
 27 models produce frequent overshooting convection whose strongest updrafts humidify the  
 28 TTL and are its main source of frozen water. Inter-model differences in cloud proper-  
 29 ties and convective injection exceed differences between land and ocean regions in each  
 30 model. We argue that global storm-resolving models can better represent tropical cir-  
 31 rus and deep convection in present and future climates than coarser-resolution climate  
 32 models. To realize this potential, they must use available observations to perfect their  
 33 ice microphysics and dynamical flow solvers.

34 **Plain Language Summary**

35 High-altitude tropical cirrus (ice) clouds influence the earth's climate by reflect-  
 36 ing sunlight, trapping upwelling radiative energy from the earth's surface, and affecting  
 37 the temperature and humidity of the upper atmosphere. These clouds are initiated by  
 38 systems of strong thunderstorms, whose most vigorous updrafts loft water vapor and ice  
 39 high into the atmosphere. Computer models used to study the global climate struggle  
 40 to accurately represent tropical thunderstorms because their updrafts are far narrower  
 41 than the width of a modeled grid cell. Models with very fine grids can better represent  
 42 the air flows that form these clouds. We investigate how well several fine-grid models re-  
 43 produce observed characteristics of tropical thunderstorm systems and cirrus. We find  
 44 generally good agreement but also substantial differences between individual models, mainly  
 45 because of their diverse ways of representing ice and snow formation and their evolution.  
 46 With further observationally-motivated improvements, such fine-grid models should en-  
 47 able more reliable simulations of the role of tropical cirrus in our changing climate.

48 **1 Introduction**

49 Upper-tropospheric cirrus influence the climate through local radiative heating. These  
 50 cirrus extend throughout the tropics and can be advected up to 1000 km during their  
 51 long lifetimes (Luo & Rossow, 2004). Jensen et al. (1996a) found that very thin cirrus  
 52 can warm the surrounding atmosphere by a few Kelvins per day. Due to the prevalence  
 53 of the cirrus, this heating alters the top-of-atmosphere radiation balance (Lee et al., 2009;  
 54 Haladay & Stephens, 2009).

55 Tropical cirrus in the upper troposphere are strongly related to deep convection.  
 56 Areas with a high occurrence of cirrus clouds are often collocated with frequent convec-  
 57 tion (e.g., Lee et al., 2009; Sassen et al., 2009; Schoeberl et al., 2018). Near the tropopause,  
 58 cirrus can form through convective anvil detrainment as well as in situ ice nucleation (Jensen  
 59 et al., 1996b). Some of the cirrus formed in situ may also be related to convection if the  
 60 ice nucleation results from cooling caused by gravity wave perturbations (Dessler et al.,  
 61 2006; Jensen et al., 2016; Krämer et al., 2016). Pervasive, mostly optically thin cirrus  
 62 characterize the transition region between the upper troposphere and lower stratosphere,  
 63 known as the tropical tropopause layer (TTL; see review article by Fueglistaler et al.,  
 64 2009). Several definitions for the TTL boundaries have been proposed in the literature;

here, we take the TTL to be the 14–18 km layer in the tropics. The formation and maintenance of TTL cirrus are of particular interest to us. Like other upper-tropospheric cirrus, TTL cirrus are associated with deep convection. Overshooting convection that reaches into the TTL is especially important for TTL cirrus as it injects water vapor and ice crystals into the layer to support cirrus formation (e.g., Massie et al., 2002; Luo & Rossow, 2004; Mace et al., 2006; Krämer et al., 2016) and can ultimately alter the TTL composition (Fierli et al., 2011; Virts & Houze, 2015). Additionally, Jensen et al. (1996a) determined that cirrus near the tropopause formed outside of convection act to dehydrate the stratosphere. Both TTL cirrus and changes in stratospheric water vapor concentrations radiatively impact large-scale upper-atmospheric circulations and the global climate (Solomon et al., 2010).

Overshooting convection drives water transport into the upper troposphere and is a major issue for global climate models (GCMs) in simulating tropical cirrus clouds (Fueglistaler et al., 2009). Deep convection is not resolved by the typical GCM horizontal grid spacings of 25–200 km and must be parameterized, which is notoriously challenging due to the complex small-scale structure of deep convection. The parameterizations inevitably lead to substantial biases and intermodel differences in simulated deep convection and related clouds. For instance, most GCMs simulate the diurnal cycle of convection over land poorly, with a maximum in precipitation often occurring too early in the day (Yang & Slingo, 2001; Khairoutdinov et al., 2005; Chao, 2013). An accurate diurnal cycle is needed to simulate tropical cirrus because the timing of anvil detrainment may affect the cirrus characteristics and thus their radiative effects (Sokol & Hartmann, 2020). Land convection is particularly important for TTL cirrus because it penetrates the TTL more often (Liu & Zipser, 2005) and is more intense than ocean convection (Yang & Slingo, 2001; Zipser et al., 2006). However, different convective parameterizations in GCMs disagree on the representation of convective fluxes and often struggle to reproduce convection that overshoots the cold point (Arteta et al., 2009).

Cloud-resolving models (CRMs) have sufficiently fine horizontal grid spacings to explicitly resolve deep convection without parameterization. An early CRM study by Bechtold et al. (2004) found that the precipitation maximum over tropical land realistically shifted to later in the day with nonparameterized deep convection. This improvement in the simulated diurnal cycle has been reproduced by numerous studies (e.g., Duda & Gallus, 2013; Berthou et al., 2019).

Increased computing power has since allowed for the development of global storm-resolving models (GSRMs), global CRMs of 1–5 km horizontal grid resolution, that can resolve individual convective storms. Recently, several GSRMs were brought together as part of the Dynamics of the Atmospheric general circulation Modeled On Non-hydrostatic Domains (DYAMOND) project (Stevens et al., 2019). The DYAMOND project provides a novel opportunity for the intercomparison of TTL cirrus and convection modeled at such high resolutions. Because of the expected improvements from explicitly simulating deep convection, the DYAMOND models have the potential to more accurately model tropical cirrus in the upper troposphere and TTL in a changing climate. But is this potential realized, even in the present climate that we can observe? Other parameterizations still needed in GSRMs, especially ice microphysics, could still be major sources of model error. GSRM fidelity in accurately simulating strong grid-scale convective updrafts and downdrafts also needs to be assessed.

The goal of this paper is to use a variety of observations, mainly from satellites, over representative land and ocean regions to assess how well tropical deep convection and convectively generated cirrus are simulated in the DYAMOND GSRMs. In Part II of this paper, Turbeville et al. (2021) analyze the full life cycle of tropical cirrus and their radiative effects in the DYAMOND GSRMs. The remainder of the paper is organized as follows: Section 2 provides an overview of the methods, including descriptions of the models, datasets, and study regions. We assess the fidelity of the DYAMOND models

in simulating both land and ocean convection in section 3. We examine the differences in the model output of microphysical variables related to cirrus in section 4. In section 5, we relate deep convection to the simulated cirrus by analyzing the convective injection of water vapor and ice into the TTL. Finally, section 6 summarizes and discusses the results and their implications for our understanding of modeling tropical cirrus.

## 2 Methods and Data

### 2.1 DYAMOND Models

The DYAMOND initiative brought together nine different GSRMs with 5 km or finer horizontal grid spacings and explicit, nonparameterized deep convection (Stevens et al., 2019). These GSRMs each have their own specific design described in detail in Stevens et al. (2019), but all models were initialized from the same meteorological analysis and run freely for a total of 40 days from 1 August to 10 September 2016. In addition to the high spatial resolution, the DYAMOND GSRMs also have high temporal resolution, with output saved every 15 minutes for 2D fields and every 3 hours for 3D fields.

Our analysis focuses primarily on the four models: NICAM, FV3, ICON, and SAM (starred models in Table 1). Hereafter we refer to these models collectively as NFIS. This limited subset of models allows for a detailed, in-depth evaluation of such high resolution simulations while maintaining a manageable output volume. To place the NFIS models into context with the rest of the intercomparison, we also evaluate the output of certain 2D fields for the other DYAMOND models: IFS, ARPNH, MPAS, and UM (Table 1). We have omitted the ninth model, the Goddard Earth Observing System (GEOS), because the saved DYAMOND run included a poor implementation of its microphysics scheme that distorted the model results.

**Table 1.** List of DYAMOND Models

Model name	Abbreviation	Horiz. grid spacing (km)
Non-hydrostatic Icosahedral Atmospheric Model	NICAM*	3.5
Finite-Volume Cubed-Sphere Dynamical Core	FV3*	3.3
Icosahedral Non-hydrostatic Model	ICON*	2.5
Global System for Atmospheric Modeling	SAM*	4.3
Integrated Forecast System	IFS	4.8
ARPEGE-NH	ARPNH	2.5
Model for Predicting Across Scales	MPAS	3.8
United Model	UM	7.8

*Note.* We focus on the first four models (starred) and use the others for comparisons of certain 2D variables.

We have analyzed the NFIS models at their native grid scales where possible; however, some interpolation was necessary for ICON and FV3. ICON output is saved on an icosahedral grid, so for spatial plots all variables were first interpolated via nearest neighbors onto the finest latitude-longitude grid permitted by the number of cells. For FV3, the 3D hydrometeor profiles, 2D integrated water paths, and pressure were regridded through first-order conservative remapping onto a regular latitude-longitude grid while all other variables were saved on the native cubed sphere grid. These regridded variables had a larger number of cells in the study regions than the native variables, so for any analysis involving both types, all variables were first aligned onto a new latitude-longitude grid through nearest neighbors interpolation. In addition, FV3 uses a hybrid pressure-sigma vertical coordinate and the altitude was only saved on a limited number of pressure levels. We calculated a regional-mean altitude of all model levels from horizontal regional

averages of pressure, temperature, and specific humidity by integrating the hypsometric equation up from the known horizontal-mean surface elevation and pressure.

Most DYAMOND models have one-moment microphysics schemes, which partition the frozen water into cloud ice, snow, and graupel. Unlike the models, satellite measurements generally cannot distinguish between the types of frozen hydrometeors. The observed “ice” is most accurately compared to the total sum of what each model defines as cloud ice, snow, and graupel, which we refer to here as the total frozen water. In addition to the 3D profiles of cloud ice, all models except ARPNH and UM saved output for the 2D column-integrated ice water path (IWP), snow water path (SWP), and graupel water path (GWP), whose sum we call the frozen water path (FWP). However, NICAM is the only model that also saved the 3D output of snow and graupel, so we can only directly compare 3D profiles of the observed frozen water content (FWC) to NICAM output. Section 4 further discusses the implications of this limitation.

Finally, we have omitted the first 48 hours of each model from any averaging or sampling to avoid contamination from the spin-up period, which includes an initial shock in precipitation in NICAM. Therefore, “time-mean” refers to the average of days 3–40 in each DYAMOND model run (i.e., 3 August to 10 September 2016).

## 2.2 Datasets

Since the DYAMOND models were run freely, they will not reproduce specific, observed weather systems after the first few days. Therefore, we assess model fidelity by comparing time means and distributions of their output to a set of observational and reanalysis data from the same time of year.

We take FWC measurements from DARDAR-CLOUD v2.1.1, which combines radar and lidar retrievals from CloudSat and CALIPSO (Delanoë & Hogan, 2008, 2010). These satellites, part of NASA’s A-Train constellation, cross the equator at approximately 01:30 and 13:30 local time for nighttime and daytime measurements, respectively (Stephens et al., 2002). The combination of radar and lidar data in DARDAR (raDAR-liDAR) capitalizes on the detection strengths of both instruments to enable retrievals in areas of deep convection as well as thin cirrus. The DARDAR data have a 1.1 km horizontal grid spacing and 60 m vertical grid spacing (e.g., Sokol & Hartmann, 2020). We use FWC retrievals from July-August-September (JAS) 2009, which corresponds to the season of the DYAMOND simulations. The data are then integrated vertically to compute the observed FWP. Although solar noise increases the uncertainty in lidar measurements during the day, we include both daytime and nighttime retrievals to avoid diurnal bias.

For precipitation, we build an 11-year climatology during the DYAMOND period by merging estimates from 1 August to 10 September 2006–2016. We use the Tropical Rainfall Measurement Mission (TRMM) Multi-satellite Precipitation Analysis (TMPA) 3B42 version 7 product, which contains 3 hourly data at a spatial resolution of 0.25° (Huffman et al., 2007, 2010). This product combines microwave and infrared rainfall estimates with precipitation gauge measurements using the algorithm described by Huffman et al. (2007) with modifications for the current version detailed in Huffman and Bolvin (2018).

We obtain retrievals of outgoing longwave radiation (OLR) from the sun-synchronous Clouds and the Earth’s Radiant Energy System (CERES) satellite for JAS 2007–2010. The CERES data are contained in the CALIPSO, CloudSat, CERES, and MODIS merged data product (CCCM) described by Kato et al. (2010, 2011). CERES has a ~20 km footprint and also belongs to the A-Train constellation.

For temperature and humidity, we use the high-resolution European Center for Medium Range Weather Forecasts (ECMWF) Reanalysis v5 (ERA5) from 1 August to 10 September 2016. The ERA5 dataset contains global hourly output on 37 pressure levels at a res-

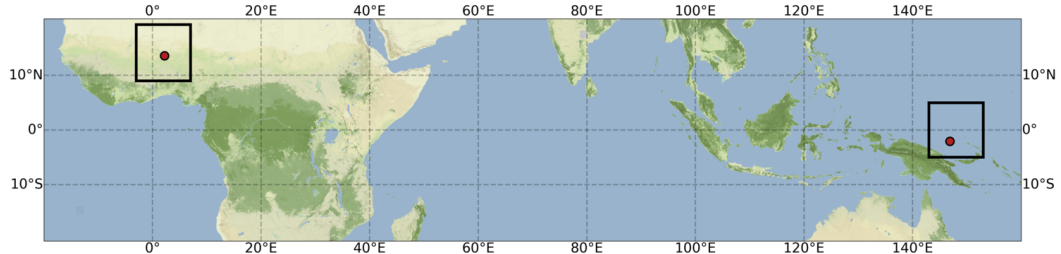


**Figure 1.** Locations of the analysis regions in (left) the Sahel,  $3^{\circ}\text{W}$ – $7^{\circ}\text{E}$ ,  $9^{\circ}\text{N}$ – $19^{\circ}\text{N}$ ; and (right) the tropical West Pacific,  $143^{\circ}\text{E}$ – $153^{\circ}\text{E}$ ,  $5^{\circ}\text{S}$ – $5^{\circ}\text{N}$ . Red dots indicate locations of the (left) AMMA and (right) ARM sites.

olution of 31 km regridded to  $0.25^{\circ}$  (Hersbach et al., 2020). We calculate the altitude of each pressure level from the ERA5 geopotential variable.

### 2.3 Study Regions

This study examines two representative  $10^{\circ}\times 10^{\circ}$  latitude-longitude regions in the tropics as shown in Figure 1: a continental area over the Sahel (SHL) in western Africa and an oceanic area over the tropical West Pacific (TWP).

The Sahel region was chosen to represent tropical land for several reasons. This area experiences frequent deep convection during the DYAMOND period when the West African Monsoon is active. Furthermore, a large proportion of overshooting convection that extends above 14 km in the tropics occurs over Africa (Liu & Zipser, 2005). The Sahel region encompasses several different climate regions, from the moist and convectively active savanna to the Sahara desert where detrainment anvils are the main cloud type during the monsoon season (Futyan et al., 2004). Finally, this region is approximately centered over the African Monsoon Multidisciplinary Analysis (AMMA) measurement site in Niamey, Niger, where the RADAGAST field campaign took place in 2006 (Slingo et al., 2008). RADAGAST generated a rich suite of measurements of the overlying atmospheric column that may in the future be climatologically compared with the DYAMOND output.

The TWP region contains frequent ocean convection, a valuable complement to the Sahel region. The TWP box is approximately centered over the Atmospheric Radiation Measurement (ARM) site in Manus, Papua New Guinea (Long et al., 2016) and is the primary study area used in Part II.

### 2.4 Mass Flux Calculation

One goal of this study is to analyze how the DYAMOND models bring the ice and moisture necessary to support cirrus cloud formation and maintenance into the TTL. To this end, we examine the vertical advective mass fluxes of frozen water and water vapor at 14 km, a representative height of the TTL base. The mass fluxes ( $F$ ,  $\text{kg m}^{-2} \text{s}^{-1}$ ) of water vapor, frozen water, cloud ice, snow, and graupel are calculated in equation (1):

$$F = w\rho q^* \quad (1)$$

Here,  $w$  is the vertical velocity ( $\text{m s}^{-1}$ ),  $\rho$  is the air density ( $\text{kg m}^{-3}$ ), and  $q^*$  ( $\text{kg kg}^{-1}$ ) is either the specific humidity for the water vapor flux or the specific water content (frozen, cloud ice, snow, or graupel) for the other fluxes. The  $w$  used in equation (1) does not include any ice fall velocity, which was not an output archived by the models. We calculate the water vapor and cloud ice mass fluxes for all NFIS models. Since FV3, ICON,

230 and SAM do not save the 3D model outputs of snow and graupel that are needed to de-  
 231 termine the total FWC, we can only calculate the frozen water, snow, and graupel mass  
 232 fluxes for NICAM.

## 233 2.5 Frozen Water Path Categorization

234 We will use the FWP to divide ice-containing air columns into three categories with  
 235 distinct physical characteristics, following Sokol and Hartmann (2020):

- 236 **Category 1:**  $\text{FWP} \geq 1000 \text{ g m}^{-2}$  (deep convection)
- 237 **Category 2:**  $10 \leq \text{FWP} < 1000 \text{ g m}^{-2}$  (thick “anvil” cirrus)
- 238 **Category 3:**  $0.1 \leq \text{FWP} < 10 \text{ g m}^{-2}$  (thin cirrus).

239 The models can simulate cirrus layers so thin that lidar cannot distinguish them from  
 240 clear sky. The lower threshold of Category 3 is chosen to exclude most such cirrus lay-  
 241 ers from our model-observation comparisons. It corresponds to a 200 m thick cirrus layer  
 242 (narrower than the 400–600 m vertical grid spacing of the NFIS models within the TTL)  
 243 with an average FWC of  $5 \times 10^{-4} \text{ g m}^{-3}$ , which Deng et al. (2013) found to be the small-  
 244 est value measurable by satellite-based lidar. Columns with  $\text{FWP} < 0.1 \text{ g m}^{-2}$  are con-  
 245 sidered to be cirrus-free.

246 The SAM 2D water paths require additional processing. These files were saved with  
 247 2-byte compression that quantizes values into integer multiples of 1/64,000th of the field  
 248 maximum. While IWP and liquid water path (LWP) can be computed by integrating  
 249 profiles of cloud ice and liquid in the 3D outputs, we statistically correct the errors due  
 250 to quantization in the snow, graupel, and rain water paths by adding random pertur-  
 251 bations to any values below  $1 \text{ g m}^{-2}$ . This categorization, as well as the SAM process-  
 252 ing, is also used to evaluate TTL cirrus in Part II.

## 253 3 Convection

254 In this section, we evaluate the performance of the DYAMOND models in simu-  
 255 lating both land and ocean convection.

### 256 3.1 Thermodynamic Background

257 Since the DYAMOND models are not nudged towards observations, they each set-  
 258 ttle into their own climates over the course of the model run. We compare the model out-  
 259 put for temperature and relative humidity to ERA5 reanalysis data in order to under-  
 260 stand the mean thermodynamic state of each model. The relative humidity with respect  
 261 to ice in the DYAMOND models was calculated using the equation for ice-saturation va-  
 262 por pressure from Murphy and Koop (2005).

263 Across both the Sahel and TWP study regions, the time-mean TTL temperature  
 264 profiles vary between the models but all lie within 5 K of the ERA5 reanalysis (Figure  
 265 2a–b). The cold point temperatures are a few degrees lower and closer to saturation in  
 266 the TWP than in the Sahel. In both regions, the cold points are located within approx-  
 267 imately 1.5 km of ERA5 and have a temperature range of about 3.5 K (Figure 2a–b).

268 Despite their microphysical diversity, the models all simulate mean relative humid-  
 269 ity profiles that scatter within ~15% of ERA5 below the cold point and fall well within  
 270 one standard deviation of the ERA5 daily mean (Figure 2c–d), which is not true of the  
 271 temperature profiles. This disagreement in temperature but not relative humidity sug-  
 272 gests that convection has a lasting influence on the TTL in the NFIS models; the mean  
 273 temperature profiles alone do not explain the relative humidity profiles, so the infrequent

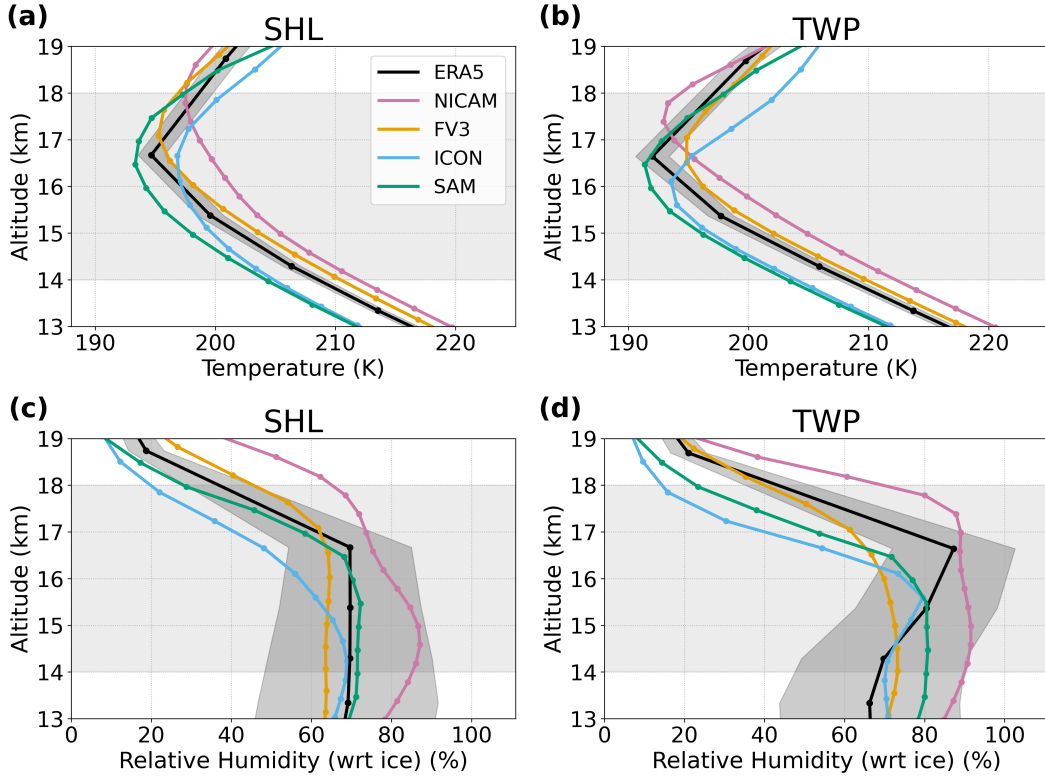


**Figure 2.** Time- and regional-mean vertical profiles of (top) temperature and (bottom) relative humidity with respect to ice for the (left) Sahel and (right) TWP for the NFIS models and ERA5 reanalysis data. The standard deviation of the daily mean ERA5 data is shaded in dark gray. The TTL is shaded in light gray.

periods of deep convection likely help to humidify the upper troposphere to around 70–90%, consistent with Ueyama et al. (2018).

### 3.2 Accumulated Precipitation

The DYAMOND models scatter around the observed accumulated precipitation in both regions, with generally higher precipitation over the TWP (Figure 3b) than the Sahel (Figure 3a). The ratio of TWP to Sahel 40-day accumulated precipitation ranges considerably from 1.0 (ARPNH, IFS) to 3.6 (UM), compared to an 11-year TRMM climatological estimate of 1.6 for the DYAMOND period in 2006–2016. Since the models are free-running and a 40-day average is short, this ratio may not be fully representative of each model’s climatological behavior, but Figure 3 suggests some models systematically precipitate more than others in each region.

The DYAMOND models as a whole reasonably simulate the total precipitation in both regions with most model accumulation falling within the 11-year TRMM climatological range. Among the NFIS models, none simulate precipitation notably better than the others. SAM consistently accumulates about 50% more precipitation than the climatological rate. NICAM, FV3, and ICON are very close to the climatological rate in the Sahel, but ICON underestimates and FV3 overestimates precipitation in the TWP. The strong NICAM precipitation on 1 August in the TWP results from the initial shock (see section 2.1); thereafter, the total accumulated precipitation in NICAM tracks the top end of the TRMM range.

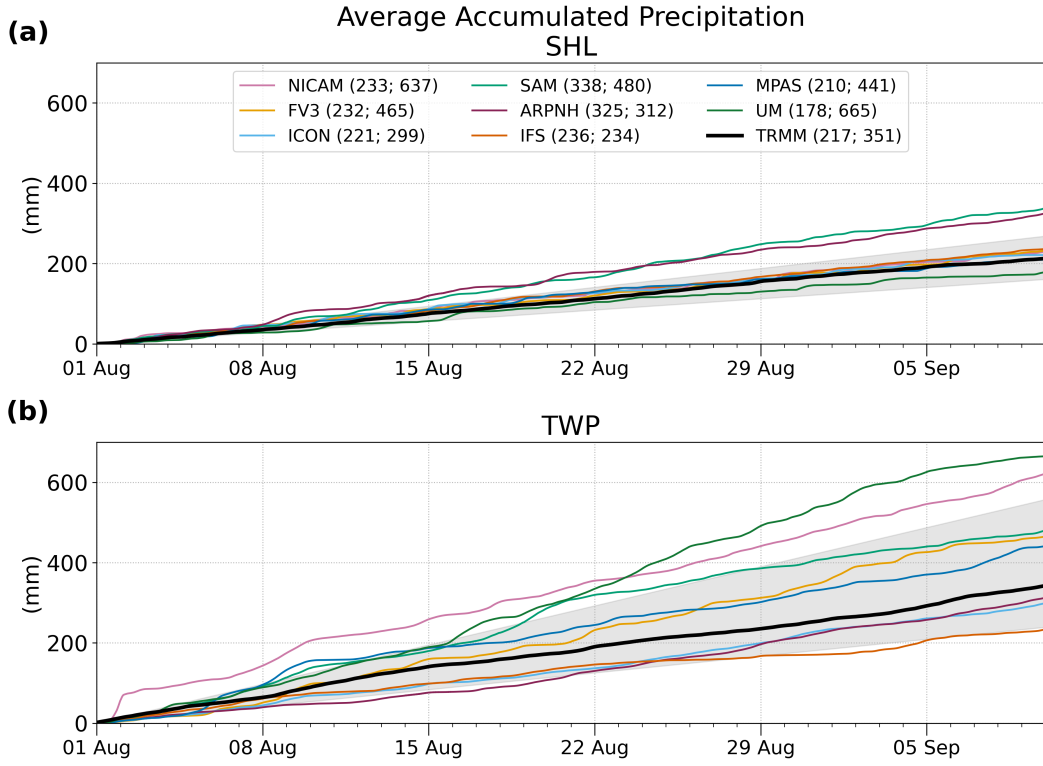


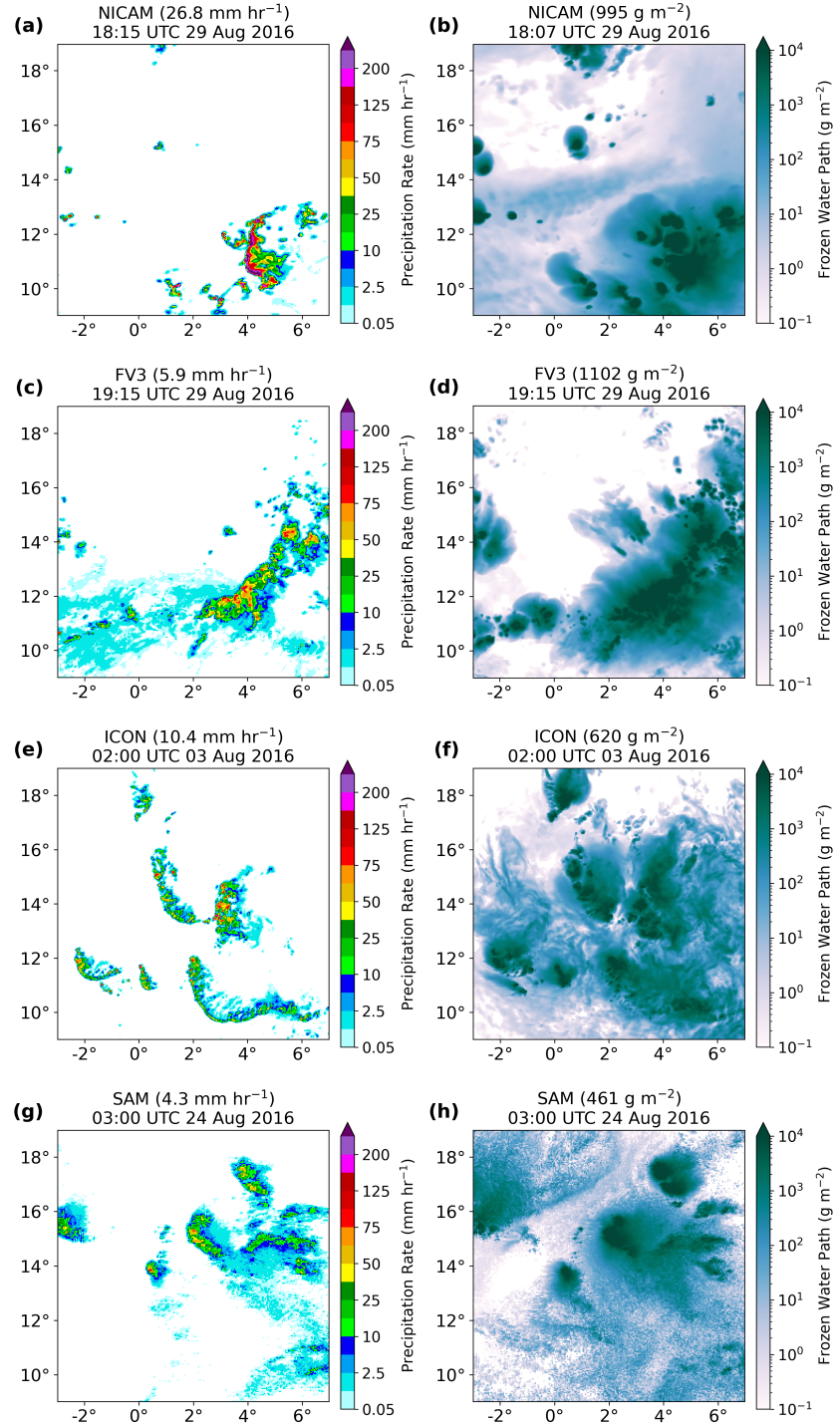
**Figure 3.** Regional-mean accumulated precipitation at each time step for the (a) Sahel and (b) TWP. The black line represents the 2006–2016 TRMM climatological mean accumulation during the DYAMOND time period. The gray shading shows the range in accumulation observed by TRMM over this 11-year period. The numbers in the legend are the 40-day accumulations in (left) the Sahel and (right) the TWP in mm.

294

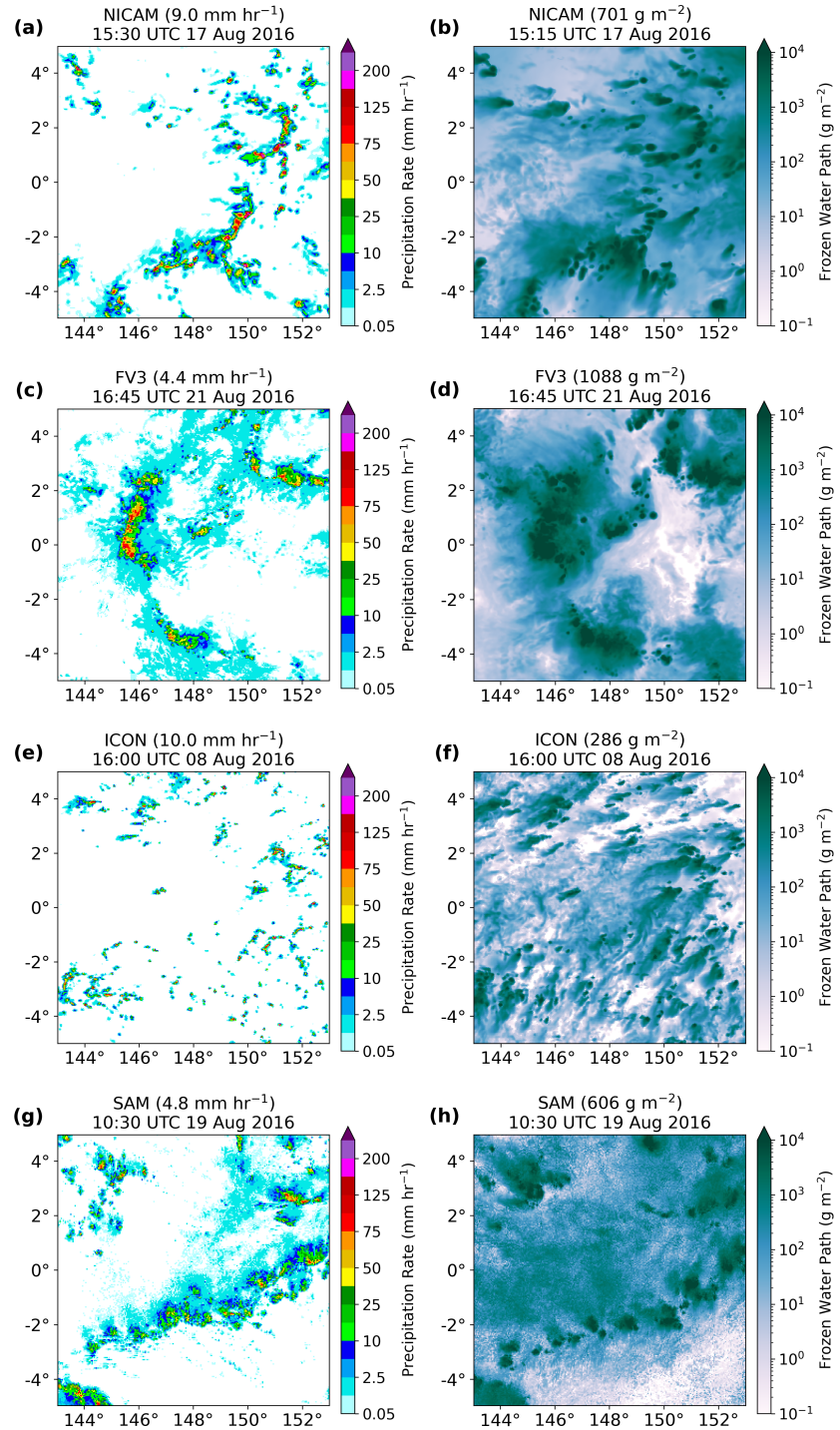
### 3.3 Texture of Convection

295  
296  
297  
298  
299  
300

The “texture” (fine-scale morphology) of precipitation is an illuminating diagnostic of how well models simulate the details of convection and differences between land and ocean regions (Inoue et al., 2008). Figures 4 and 5 show characteristic snapshots of precipitation in the NFIS models for the Sahel and TWP, respectively. For each model, we have selected the output times with the maximum regional-mean precipitation rate after the 48-hour spin-up period.



**Figure 4.** Snapshots of (left) precipitation rate and (right) frozen water path (FWP) over the entire  $10^\circ \times 10^\circ$  box in the Sahel. Rates below  $0.05 \text{ mm hr}^{-1}$  and FWPs below  $0.1 \text{ g m}^{-2}$  are masked. The numbers in each panel title indicate the regional-mean precipitation rate or FWPs for each snapshot. The timing of the saved FWP output for NICAM is offset from the precipitation by 7.5 minutes.

**Figure 5.** As in Figure 4, but for the TWP.

In the Sahel, the NFIS models all produce realistic squall lines with narrow, short-lived bands of precipitation that are characteristic of the region (Figure 4) (Redelsperger & Lafore, 1988; Redelsperger et al., 2002). However, FV3 and SAM have an excess of light precipitation that is uncharacteristic of the Sahel (Figure 4c, g). Much of this light precipitation comes from shallow cumulus clouds (parameterized in FV3) which are not

306 apparent in the FWP snapshot. The areal extent of thin cirrus clouds in NICAM is much  
 307 larger than in the other models (Figure 4b). In all models, there is a strong collocation  
 308 between the FWP and precipitation fields in which the precipitation tracks with the cloud  
 309 field.

310 Similarly in the TWP, NICAM, FV3, and SAM reproduce the large, widespread  
 311 convective systems typically observed over tropical oceans (Figure 5) (Bousquet & Chong,  
 312 2000). FV3 and SAM again have expansive regions of unrealistically light precipitation,  
 313 but to a lesser extent than in the Sahel. The precipitation in ICON consists of small pock-  
 314 ets of “popcorn” convection scattered throughout the region (Figure 5e). As in the Sa-  
 315 hel, areas of intense precipitation collocate with higher FWPs. In NICAM, the entire  
 316  $10^\circ \times 10^\circ$  TWP box has frozen water in the atmospheric column (Figure 5b). Although  
 317 there is diversity in the details of precipitation and FWP in individual models that is  
 318 generally consistent in the Sahel and TWP, the models simulate a reasonable texture of  
 319 both precipitation and convection and capture the expected regional differences in land  
 320 and ocean convection.

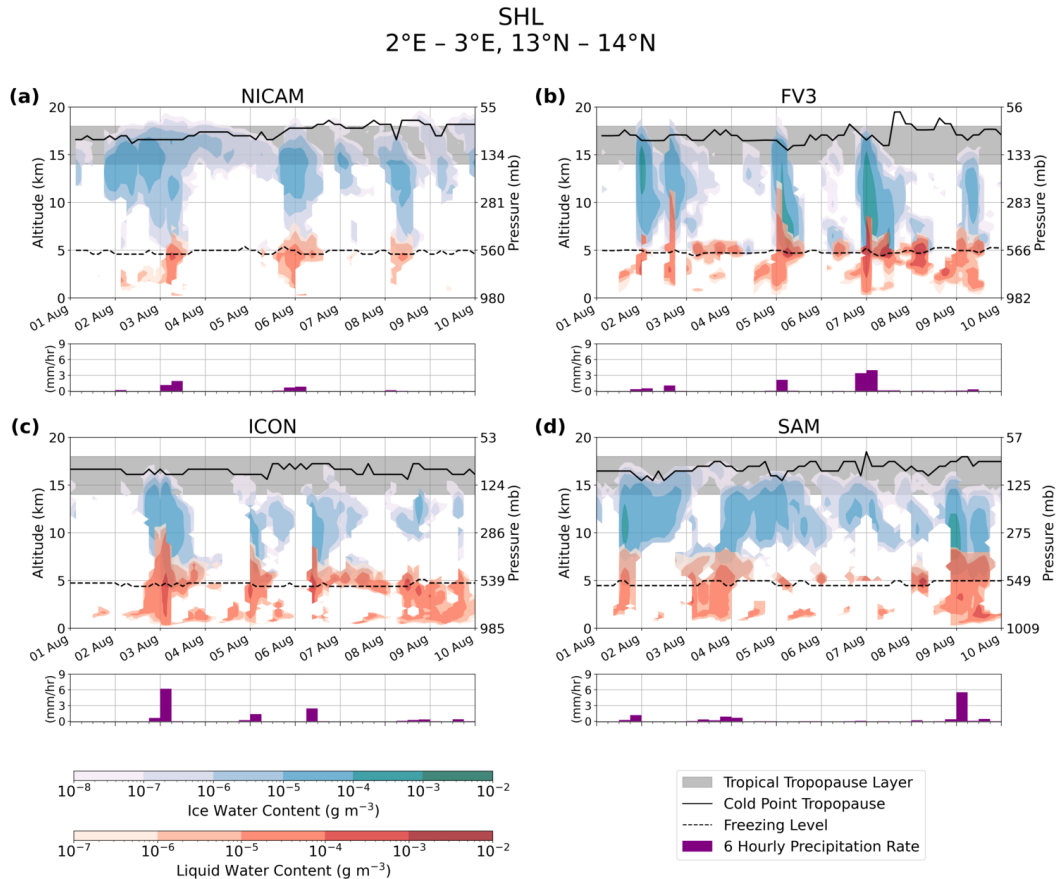


**Figure 6.** Time series of the convective cloud structure for the NFIS models in the Sahel. Ice water content is shaded in blue and liquid water content is shaded in red. Purple bars indicate the 6 hourly precipitation rate. The solid black line shows the cold point tropopause while the dashed black line shows the melting level. The TTL is shaded in gray. Model output is averaged over a  $1^\circ \times 1^\circ$  box located at  $2^\circ\text{E}$ - $3^\circ\text{E}$ ,  $13^\circ\text{N}$ - $14^\circ\text{N}$ , approximately centered over the AMMA site in Niamey, Niger. The first 48 hours (1–2 August) should be regarded as the model spin-up period.

As with precipitation, the vertical structure of convective clouds is plausibly simulated in the NFIS models, but with clear intermodel differences. Figures 6 (SHL) and 7 (TWP) show time series of the vertical cloud structure within a  $1^\circ \times 1^\circ$  box during the first 10 days of the model run. These figures highlight the qualitative differences in land and ocean convection (e.g., Liu et al., 2007), which the models capture nicely. Convection in the Sahel (Figure 6) is more sporadic and often deeper than in the TWP, where convection is nearly constant (Figure 7). The simulated deep convective clouds in the Sahel lack support from low clouds below the melting level in NICAM, FV3, and ICON.

For all models, the cloud structures and 6 hourly precipitation rates are consistent with the precipitation texture in Figures 4 and 5. The excessive TTL ice is consistent with the pervasive FWP in NICAM in both regions. For ICON in the TWP, the precipitation rates are substantially lower than in the other models, which agrees with the popcorn texture in the FWP and precipitation snapshots. The more intense convection in FV3 in both regions is evident in the depth of convection in Figures 6b and 7b as well as the higher FWPs within the deep convective cells in Figures 4d and 5d.

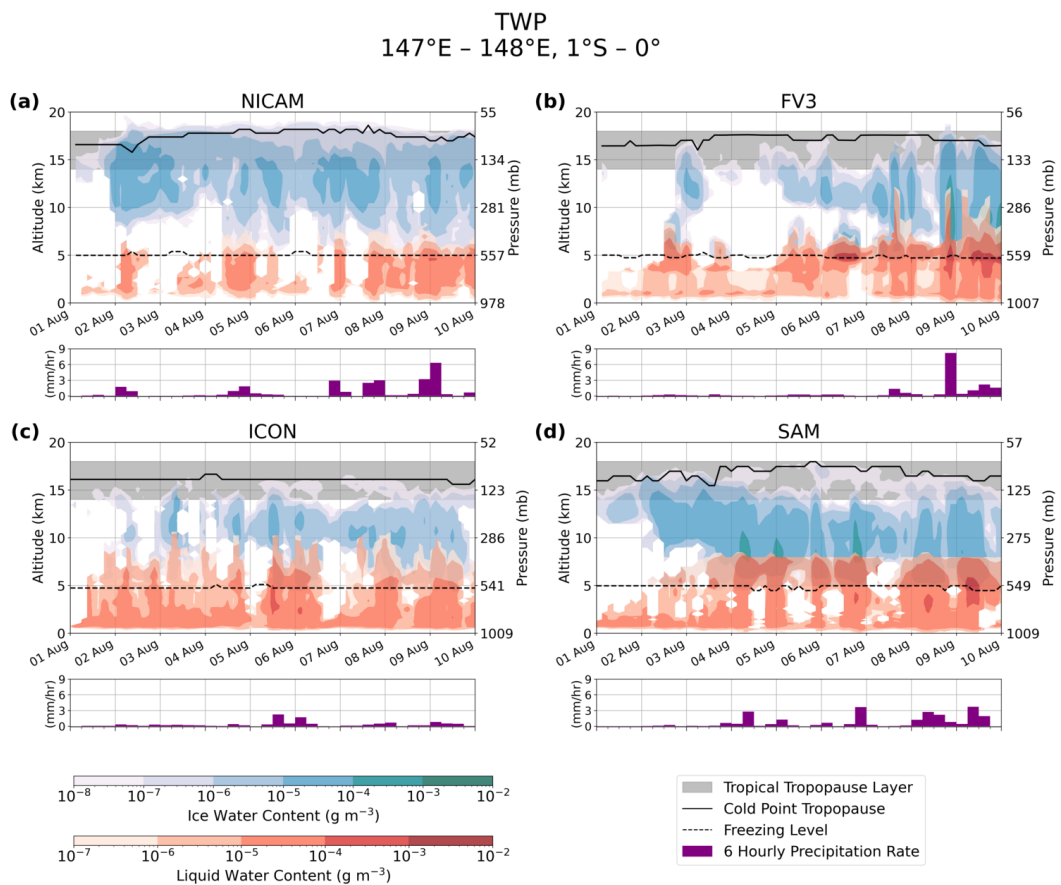


**Figure 7.** As in Figure 6, but for the TWP. Model output is averaged over a  $1^\circ \times 1^\circ$  box located at  $147^\circ\text{E}$ – $148^\circ\text{E}$ ,  $1^\circ\text{S}$ – $0^\circ$ , approximately centered over the ARM site in Manus, Papua New Guinea.

All NFIS models have overshooting convection in the Sahel, which often penetrates past the cold point in NICAM and FV3 (Figure 6a–b). As in the average temperature profiles (Figure 2a–b), ICON places the cold point tropopause lower in the TTL than NICAM, FV3, or SAM. The cold points within the Sahel  $1^\circ \times 1^\circ$  box vary more over

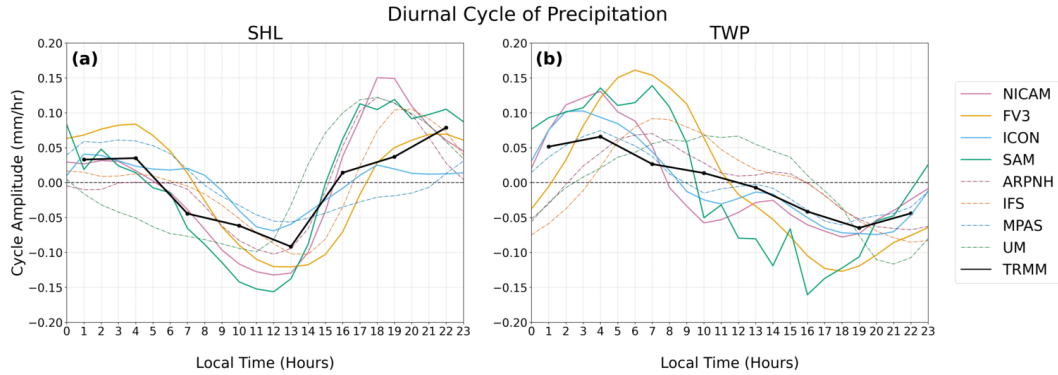


**Figure 8.** Amplitude of the regional-mean diurnal cycle of precipitation in (a) the Sahel and (b) the TWP for all DYAMOND models and for the 2006–2016 TRMM climatology. Precipitation rates are averaged at each hour for days 3–40 of the model run.

time than in the TWP. The frequency of convection reaching past the cold point in the models is surprising because very few precipitation features observed in the tropics extend above the lapse rate tropopause level (Liu & Zipser, 2005).

The typical vertical cloud structure differs between models. NICAM contains significantly more ice in the TTL than any of the other models (Figure 6a). Much of this additional ice comprises anvil or cirrus clouds with a low FWC. For FV3 in the Sahel (Figure 6b), convection reaches higher than other models, occasionally penetrating above 18 km. As shown in Figure 4c, the squall lines in ICON are followed by a region of lighter precipitation; this feature is apparent in the cloud structure where regions of high liquid water content indicative of low liquid clouds follow the convective cores near the melting level (Figure 6c). SAM is marked by persistent thick ice clouds with tops extending into the TTL (Figure 6d). Some of these clouds are thick anvils detaining off of the convective cores, but others appear detached with little liquid cloud below.

The vertical cloud structure in the TWP generally matches the qualitative texture expected of ocean convection, but with model-specific biases similar to the Sahel. NICAM has relatively little liquid cloud but persistent TTL ice up to an altitude of 18 km (Figure 7a). The ice within the TTL is almost entirely located above or near the tops of deep convective cores, whereas in the Sahel there are more frequent detached cirrus and anvils. ICON has a higher concentration of liquid water to support the ice cloud than in any other model, with supercooled liquid at altitudes as high as 10 km in updrafts (Figure 7c). SAM (Figure 7d) also has a lot of low liquid cloud beneath the deep convective clouds but has much more FWC than ICON in these columns, as in the Sahel (Figure 6d). These intermodel differences are also apparent in the joint albedo-OLR histograms analyzed in Part II.

### 3.4 Diurnal Cycle of Precipitation

The timing and amplitude of the 38-day diurnal cycle of precipitation for all models is similar to the TRMM 2006–2016 climatology, especially in the Sahel (Figure 8). Simulated rainfall peaks 2–3 hours too early in the Sahel (Figure 8a), but 2–3 hours too late in the TWP (Figure 8b). Nevertheless, the explicit deep convection in the DYAMOND GSRMs vastly reduces known biases in the diurnal timing of precipitation over land in GCMs (Bechtold et al., 2004).

## 371 4 Microphysics

372 Next, we examine the differences in the model output of microphysical variables,  
 373 both within the TTL and integrated over the entire grid column.

### 374 4.1 Frozen Water Content and TTL Composition

375 NICAM is the only DYAMOND model for which we have the 3D graupel and snow  
 376 output needed to plot their horizontally-averaged profiles. The vertical profiles of ice wa-  
 377 ter content (IWC), IWC + snow water content (SWC), and IWC + SWC + graupel wa-  
 378 ter content (GWC) for NICAM are plotted alongside DARDAR-estimated FWC in Fig-  
 379 ure 9a. Cloud ice dominates in the TTL, while snow and graupel peak at 6–7 km, just  
 380 above the melting level. NICAM’s total FWC peaks around the same level as the ob-  
 381 servations, but is overestimated. In the TWP, NICAM has much larger FWC on aver-  
 382 age at all levels than in the Sahel, but the relative levels and magnitudes of IWC, SWC,  
 383 and GWC have the same trend across regions (see Figure S1).

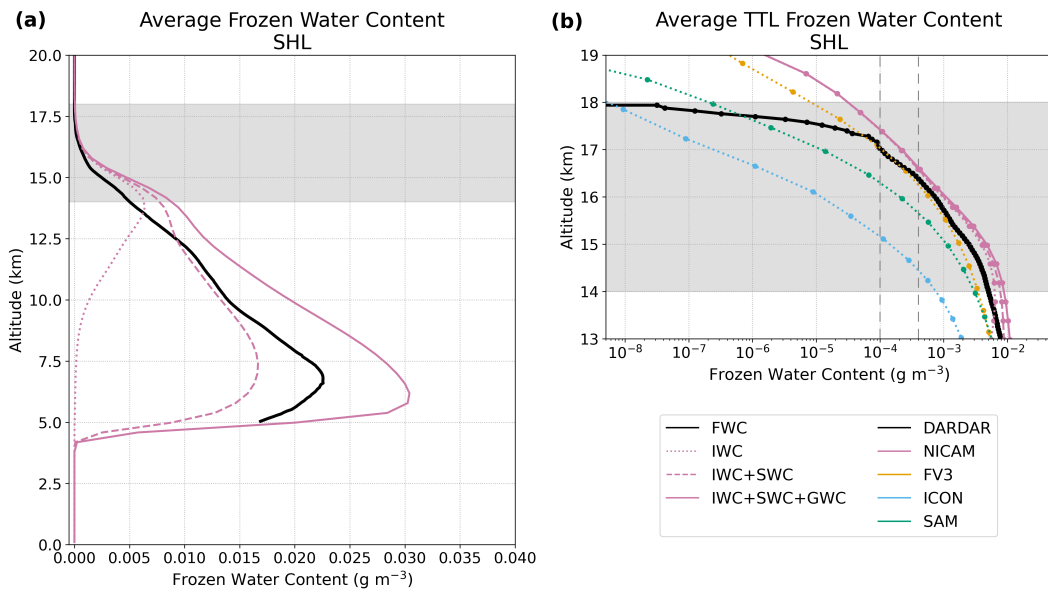


**Figure 9.** Area- and time-mean vertical profiles of frozen water contents (FWCs) in the Sahel. (a) Ice (dotted pink line), ice + snow (dashed pink line), and ice + snow + graupel (solid pink line) water contents for NICAM. The DARDAR FWC profile is shown in black. (b) Ice water content (dotted lines) for all NFIS models; ice + snow (dashed pink line) and ice + snow + graupel (solid pink line) water contents for NICAM; and DARDAR FWC (solid black line). Note that the x-axis of panel (b) is logarithmic. The dashed vertical lines indicate the approximate detection limits of the lidar at night ( $1 \times 10^{-4} \text{ g m}^{-3}$ ) and during the day ( $4 \times 10^{-4} \text{ g m}^{-3}$ ) (Avery et al., 2012).

384 Inside the TTL, the main frozen condensate type is cloud ice, which was archived  
 385 for all four NFIS models. Thus, we compare the model IWC profiles in the TTL to DAR-  
 386 DAR. NICAM, FV3, and SAM scatter within a plausible range around the observational  
 387 estimate between 14–17 km. The FV3 IWC profile is closest to the data, while SAM has  
 388 lower IWCs and NICAM has slightly higher IWCs. ICON greatly underestimates the  
 389 observational profile of IWC throughout the entire TTL. For NICAM, the total FWC  
 390 is slightly larger than the IWC at 14 km, but the contributions of snow and graupel be-

come negligible above  $\sim 17$  km. It is unclear if adding snow and graupel would make up for the differences in IWC between models seen in Figure 9b.

#### 4.2 Vertically Integrated Water Paths

In addition to IWP, GWP, and SWP, the DYAMOND intercomparison stored the column mass of the rain water path (RWP) and LWP. Figure 10 compares the time and regional averages of these quantities in the Sahel to DARDAR (see Figure S2 for the TWP equivalent). Since hydrometeors affect radiative fluxes, we also compare the time-mean simulated OLR to CERES CCCM data. The output for snow, graupel, and rain water paths was not saved for ARPNH or UM, so there is more frozen and liquid water in those models than shown here. These models are separated from the models with complete information by the vertical dashed lines in Figure 10.

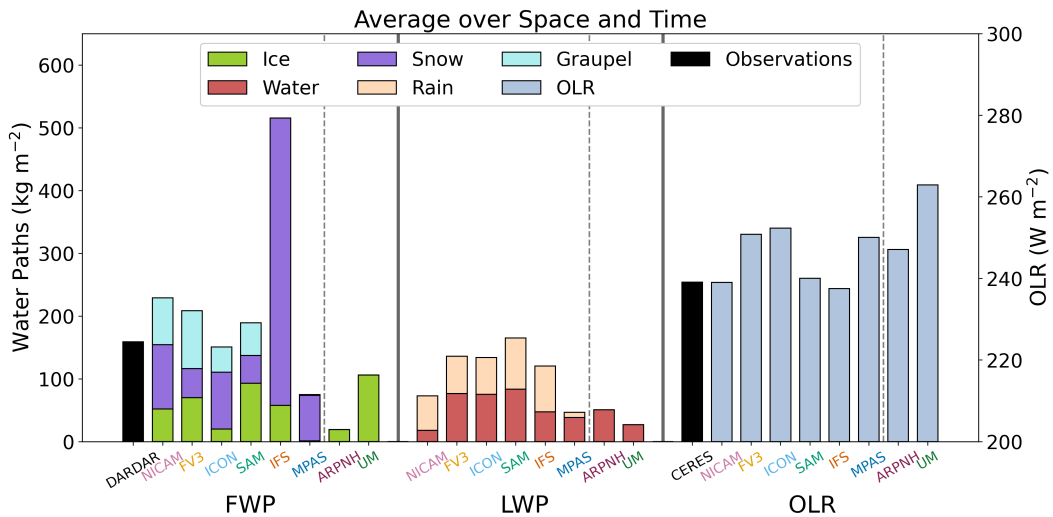


**Figure 10.** Bar chart of the time- and regional-mean frozen water paths (FWPs), total liquid water paths (LWPs), and outgoing longwave radiation (OLR) in the Sahel for all DYAMOND models. Black bars indicate observations of FWP from DARDAR and OLR from CERES. The vertical black dashed lines separate the models with complete information from those which did not save all column-integrated water paths. Note that the IFS microphysics scheme does not include graupel.

The left group of bars in Figure 10 shows a large intermodel variation in the FWP and its partitioning into frozen hydrometeor types. The FWP in IFS is almost twice that of DARDAR; however, the uncertainty in DARDAR FWP retrievals may be quite large, especially within thick clouds. In NICAM, FV3, ICON, SAM, and MPAS, the FWPs are much closer to the observed value, but the relative amounts of ice, snow, and graupel vary drastically between these models. For example, MPAS has almost no graupel or ice while ice makes up about half of the total FWP in SAM. These differences emphasize the point made in section 2.1 that the cloud ice alone does not comprise the total FWC in the models and that the hydrometeors (e.g., snow) may have a different definition in each model.

The center bars in Figure 10 compare the condensed water paths, which are more consistent across models. FV3, ICON, and IFS all have nearly identical amounts of cloud liquid and rain water, whereas NICAM and MPAS have much less.

The right bars in Figure 10 show a wide intermodel range in the average OLR. The models divide into two groups: those with average OLR close to the CERES observations (NICAM, SAM, and IFS) and those with more OLR than the observations (FV3, ICON, ARPNH, MPAS, and UM). The spread in OLR between these groups is over 25  $\text{W m}^{-2}$ , whereas the uncertainty in the CERES OLR is only 3–4  $\text{W m}^{-2}$ .

The differences in FWPs do not fully account for the OLR variation. It would be reasonable to assume that the models with more OLR have less frozen water than the others on average, but this is not always the case. For example, NICAM and IFS have a much higher FWP than DARDAR and the other models, but their average OLR is still very close to the observed mean. The mean OLR is also affected by model differences in the assumed radiative properties of each hydrometeor type in the microphysics scheme, such as the specification of their effective radii and which types are radiatively active. Additionally, mean OLR varies with the fractional coverage of clouds in each model.

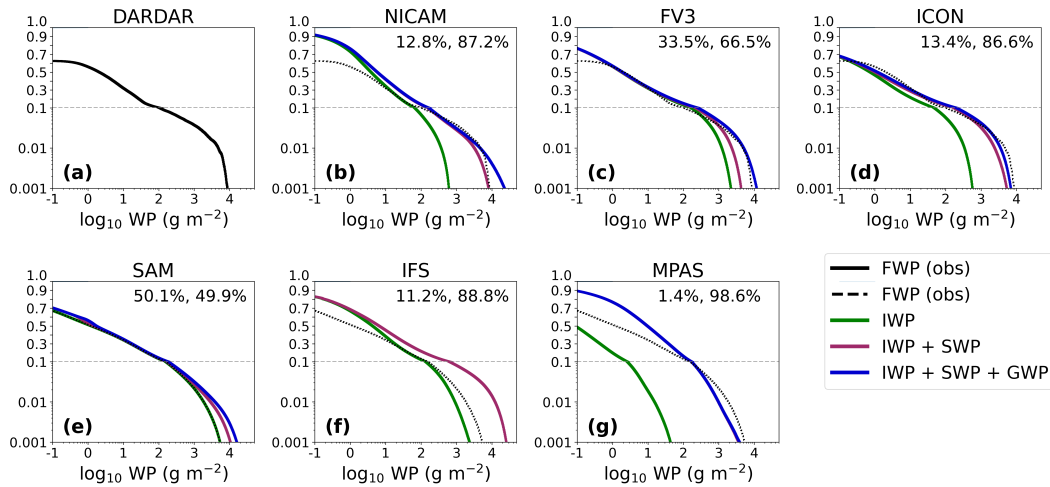


**Figure 11.** Cumulative distribution functions for ice (IWP; green line), ice + snow (IWP + SWP; pink line), and ice + snow + graupel (IWP + SWP + GWP; blue line) water paths for all models in the Sahel compared to DARDAR frozen water path observations (FWP; solid black line in a), dashed in b-g). Values are accumulated from largest to smallest. ARPNH and UM are omitted because they do not save the 2D output of column-integrated snow or graupel water paths. The y-scale is logarithmic below 0.1 and linear above; the apparent discontinuity at 0.1 is an artifact of this split. The numbers in the upper-right corner of each panel show (left) the percentage of the total FWP from ice and (right) the percentage of total FWP from snow and graupel. These numbers cannot be deduced directly from this figure but are included to emphasize the large contributions of snow and graupel. Again, note that the IFS microphysics scheme does not include graupel.

Figure 11 compares the cumulative distribution functions (CDFs) of FWP between DARDAR and the DYAMOND models. These CDFs are computed from large FWPs to small ones so that, for example, the value at  $10 \text{ g m}^{-2}$  indicates the fraction of grid columns with an FWP exceeding  $10 \text{ g m}^{-2}$ . Since we define cirrus-free columns to be those with  $\text{FWP} < 0.1 \text{ g m}^{-2}$  (see section 2.5), the CDF at  $0.1 \text{ g m}^{-2}$  is equivalent to the ice cloud fraction. The dependence of simulated FWP distribution on the different hydrometeors is shown with additional lines for the CDFs of IWP and IWP+SWP. The steeper slope approaching  $0.1 \text{ g m}^{-2}$  indicates that the smaller FWPs are more frequent in the models than in the data. Still, the smallest values of FWP may not be radiatively

437 significant, and thus the thinnest simulated cirrus may not necessarily affect the heat-  
 438 ing profiles or top-of-atmosphere radiation balance.

439 The addition of SWP and GWP highlights the substantial contribution of snow and  
 440 graupel to the overall frozen water mass in the DYAMOND models. The percentages  
 441 in each panel of Figure 11b–h list the proportion of frozen mass from ice and snow + grau-  
 442 pel, respectively. Ice is the most significant in SAM, constituting about half of the to-  
 443 tal frozen water mass. In all other models, snow and graupel make up the majority of  
 444 the frozen mass, from 66.5% in FV3 to 98.6% in MPAS. These differences in partition-  
 445 ing mostly apply to the thickest clouds with high FWPs; the IWP makes up most of the  
 446 FWP at values below  $\sim 10 \text{ g m}^{-2}$  for all except MPAS. Likewise, as shown in Figure 9,  
 447 thin cirrus within the TTL are primarily composed of cloud ice in NICAM. Neverthe-  
 448 less, the large contributions of snow and graupel further stress that we cannot directly  
 449 compare the simulated cloud ice to the observed frozen water in areas of deep convec-  
 450 tion.

451 As mentioned above, the value approached by the CDFs at  $0.1 \text{ g m}^{-2}$  represents  
 452 an ice cloud fraction. All models overestimate the observed ice cloud fraction of  $\sim 0.6$ ,  
 453 with most falling between  $\sim 0.7$  and  $\sim 0.8$ . NICAM and MPAS have a much larger ice  
 454 cloud fraction of 0.9. Qualitatively, the TWP results are similar to the Sahel (see Fig-  
 455 ure S3). All but IFS have a larger ice cloud fraction in the TWP than in the observa-  
 456 tions, but the proportion of frozen mass from snow + graupel falls within a few percent  
 457 of the Sahel values. NICAM still has the largest ice cloud fraction, which is a surpris-  
 458 ing 0.999 in the TWP (Figure S3). Overall, the microphysics schemes in the models pro-  
 459 duce consistent cloud property biases specific to each model across the tropics.

## 460 5 TTL Cirrus

461 Finally, we use the NFIS models to try to understand how TTL cirrus are related  
 462 to convection and what role convective mass fluxes play in setting the composition of the  
 463 TTL.

### 464 5.1 TTL Cirrus and Convection

465 The diurnal cycle of convection and the collocation of convection with TTL cirrus  
 466 are shown in the 40-day time series in Figure 12. Only FV3 is shown here for brevity;  
 467 equivalent figures for NICAM, ICON, and SAM are included in the Supporting Infor-  
 468 mation (Figures S4–S6). The diurnal cycle in the Sahel is much stronger and more dis-  
 469 tinct than in the TWP as expected (e.g., Yang & Slingo, 2001; Nesbitt & Zipser, 2003).  
 470 In the Sahel, the deep convection is marked by periodic bouts of very low OLR, high pre-  
 471 cipitation rates, and high IWP indicative of deep cumulonimbus towers (Figure 12a, c,  
 472 e). The regions of intense precipitation and high IWP occur more frequently and for longer  
 473 periods of time in the TWP, characteristic of the more persistent and widespread con-  
 474 vective storms observed over tropical oceans (Figure 12b, d, f). The convection and di-  
 475 urnal cycles shown in Figure 12 are qualitatively consistent with those for the other mod-  
 476 els (see Figures S4–S6) despite the intermodel differences in convection described in sec-  
 477 tion 3.

478 Peaks in TTL IWP coincide with areas of large total-column IWP (Figure 12e–h).  
 479 This suggests that the TTL ice is mostly located over deep convection, which qualita-  
 480 tively agrees with the collocation between total-column FWP and precipitation demon-  
 481 strated in Figures 4 and 5. In both regions, the NFIS models also have frequent thin-  
 482 ning anvils evident in the smaller IWPs extending away from the convective cores, but  
 483 isolated TTL cirrus are not readily apparent. Therefore, TTL ice is mostly located in  
 484 the vicinity of convection, with the majority of the ice mass concentrated directly over  
 485 deep convection.

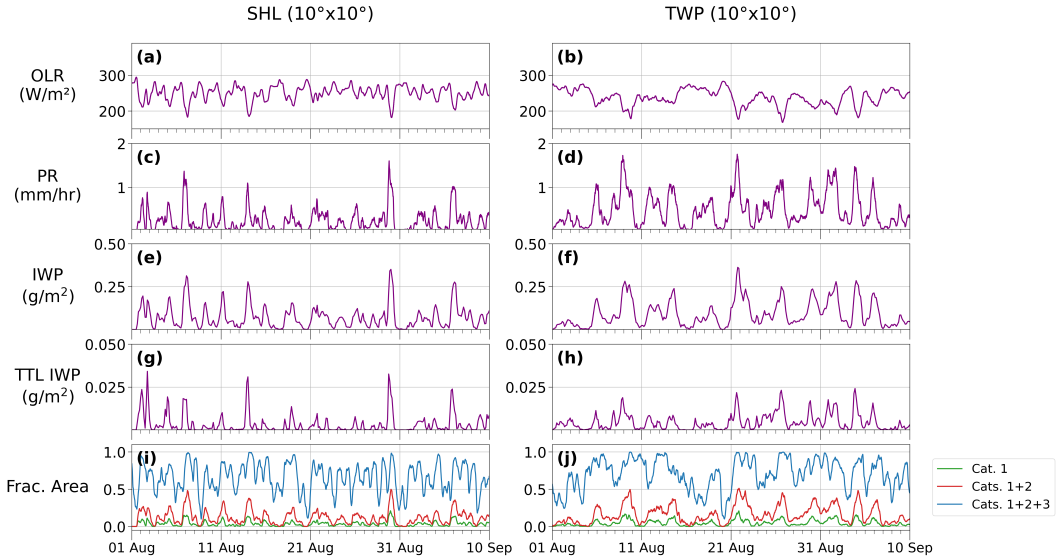


**Figure 12.** Time series for FV3 over days 1–40 of the model run: (a–b) area-mean outgoing longwave radiation (OLR); (c–d) area-mean precipitation rate (PR); (e–f) area-mean total-column ice water path (IWP); (g–h) area-mean TTL IWP; and (i–j) fractional areas of Category 1, Categories 1–2, and Categories 1–3 columns for FV3. Area-means and fractional areas are computed over the  $10^\circ \times 10^\circ$  (left) Sahel and (right) TWP regions. For the TTL IWP, ice water content is integrated between the model levels closest to 14 and 18 km, which sometimes lie slightly outside of this range.

Similarly, the area spanned by anvil cirrus in the  $10^\circ \times 10^\circ$  regions strongly correlates with that of deep convection (Figure 12i–j). Categories 1 and 2 are tightly coupled with each other and with convection in terms of low OLR, high precipitation rate, and large IWPs (Figure 12). For FV3, the fractional area of Category 2 lags behind Category 1 by about 3 hours in the Sahel and 5.5 hours in the TWP with a maximum correlation coefficient of 0.9 in both regions. The coupling between Categories 1 and 2 is qualitatively similar in NICAM, ICON, and SAM (see Figures S4–S6). Category 3 thin cirrus track more closely with deep convection and anvils in ICON and SAM while the thin cirrus columns cover almost the entire  $10^\circ \times 10^\circ$  area in NICAM. These relationships indicate that most anvils and thick cirrus are likely generated from deep convection, but other physical processes must contribute to generating and maintaining thinner cirrus.

## 5.2 Injection of Water Vapor and Frozen Water into the TTL

In Figure 13a and c, we bin cloud IWC and water vapor content (WV) in Sahel grid cells at an altitude of 14 km (the nominal base of the TTL) by the collocated vertical velocity for the NFIS models. The  $w$  bins are subjectively chosen to span the range of simulated updrafts and downdrafts; the probability distribution functions (PDFs) of vertical velocity are shown in Figure 13b. Figure 13a also shows the total FWC (i.e., including snow and graupel) for NICAM, the only model for which these variables were stored. The graupel and snow water contents may be substantial (up to 10 times larger than IWC) in areas of deep convection with strong updrafts and downdrafts. Thus, graupel and snow may dominate the vertical advective fluxes of frozen water and water vapor for NICAM (Figure 13d).

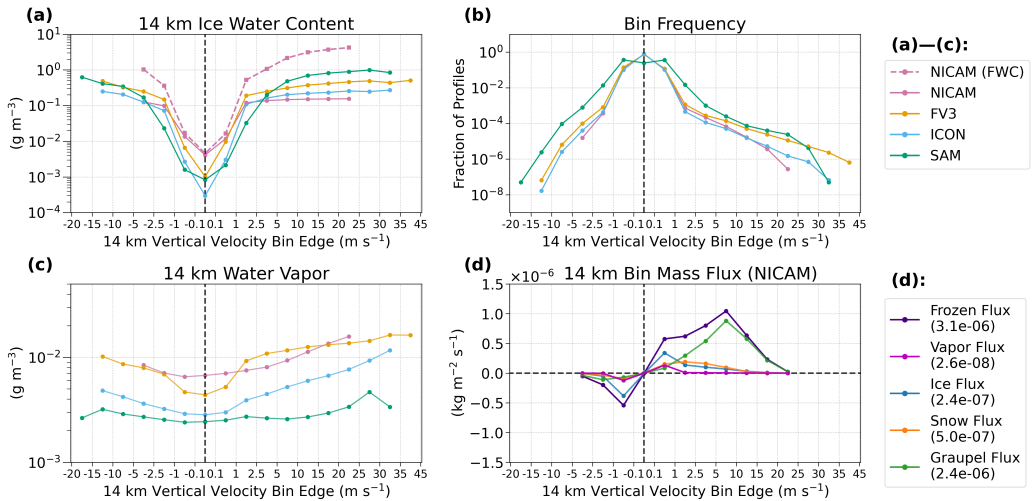


**Figure 13.** Selected variables sampled at all 14 km grid points for days 3–40 in the Sahel and averaged over vertical velocity bins: (a) cloud ice water content (pink dashed line shows NICAM frozen water content); (b) bin frequency; (c) water vapor content; and (d) frozen water, water vapor, ice, snow, and graupel mass fluxes for NICAM only.

The cloud IWC at 14 km varies greatly between models, but the relative differences across  $w$  bins are qualitatively consistent (Figure 13a). The IWC in FV3, ICON, and SAM increases by about three orders of magnitude from the weakest to strongest updrafts and downdrafts, which occur within deep convective clouds. The increase in IWC across bins is not as drastic in NICAM because its IWC is larger in the weakest  $w$  bins. For all models, the IWC is relatively symmetric between the largest positive and negative  $w$  bins, suggesting that cloud ice is typically circulated between nearby convective updrafts and downdrafts. Despite the differences in the model simulation of land and ocean convection discussed in section 3, the trends in IWC at different updraft and downdraft speeds are remarkably similar between regions (see Figure S7a).

Although the 14 km WV varies much less across  $w$  bins than the IWC, the trends differ somewhat between models (Figure 13c). For example, WV in SAM is nearly constant with  $w$ , but WV in FV3, ICON, and NICAM increases with updraft speeds. Nevertheless, the 14 km WV values are strikingly consistent; for each model and each  $w$  bin, all WV values lie within one order of magnitude from each other. As with IWC, the trends in WV are consistent across the tropics in the NFIS models (see Figure S7c).

The general shape of the vertical velocity PDF is consistent between the NFIS models, but there is intermodel spread in the infrequent extreme values (Figure 13b). Except for SAM, the models agree that in 99.9% of the grid cells,  $w$  lies within the  $-1$  to  $1$   $\text{m s}^{-1}$  bins; this is expected given the intermittency of deep convection that penetrates into the TTL. SAM simulates more 14 km updrafts and downdrafts of intermediate strength ( $1$ – $10$   $\text{m s}^{-1}$ ) than other models. SAM also produces downdrafts up to  $-20$   $\text{m s}^{-1}$  while NICAM does not simulate any downdrafts below  $-5$   $\text{m s}^{-1}$  in either region. The strongest convective updrafts reach  $45$   $\text{m s}^{-1}$  in FV3, which is  $10$ – $20$   $\text{m s}^{-1}$  larger than in the other models. The overall shape of the vertical velocity PDF is the same in the TWP as in the Sahel, but there is even more disagreement among the strongest updrafts and downdrafts (see Figure S7b). ICON and NICAM both have stronger maximum 14 km updraft speeds in the Sahel, but the updrafts in FV3 or SAM do not seem to be systematically stronger

537 in the Sahel. Overall, these differences in extreme values reflect diverse formulations of  
 538 both model dynamics and microphysics that bear further scrutiny.

539 Figure 13d shows the mass fluxes at 14 km of water vapor and frozen water for NICAM  
 540 only. The frozen mass flux is further broken down into the cloud ice, snow, and grau-  
 541 pel fluxes. Because the WV is relatively constant across  $w$  bins (Figure 13c), the  $w$ -partitioning  
 542 of 14 km water vapor flux is qualitatively similar to that of dry air and can be used as  
 543 a proxy for the total air motion. The bin-averaged vapor flux in NICAM is largest in the  
 544  $\pm 0.1\text{--}1 \text{ m s}^{-1}$  bins and negligible everywhere else (Figure 13d, dark pink line). In con-  
 545 trast, the frozen mass flux distribution (Figure 13d, purple line) is weighted toward up-  
 546 drafts exceeding  $1 \text{ m s}^{-1}$  because they contain much more frozen water than nearly qui-  
 547 escent air. In all  $w$  bins, the frozen mass flux is much larger than the water vapor flux,  
 548 consistent with the observationally-based estimates from Bolot and Fueglistaler (2021).  
 549 Similarly, the integrated mass flux values given in the lower legends of Figures 13 and  
 550 S7 show that in both regions, the upward frozen mass flux in NICAM at 14 km is much  
 551 larger than the vapor mass flux and thus is the principal source of water in the TTL. Ice  
 552 sedimentation is not considered in the distributions in Figures 13d and S7d. We presume  
 553 that the ice sedimentation quickly offsets much of this upward flux, but we still expect  
 554 that some injected frozen water remains and spreads into extensive TTL cirrus or ulti-  
 555 mately sublimates and moistens the TTL (see Figure 2c-d).

556 Among the frozen hydrometeor fluxes in NICAM (Figure 13d), cloud ice dominates  
 557 in the  $\pm 0.1 \text{ m s}^{-1}$  bins that represent the vast majority of the grid points over time (Fig-  
 558 ure 13b). In the  $1$  to  $15 \text{ m s}^{-1}$  bins, cloud ice and snow fluxes make up a small but nearly  
 559 equal proportion of the total frozen mass flux. At updrafts stronger than  $5 \text{ m s}^{-1}$ , how-  
 560 ever, the graupel flux constitutes nearly all of the frozen mass flux. In the TWP, there  
 561 is less upward frozen mass flux overall. The graupel flux there makes up a much smaller  
 562 component of the total bin-integrated frozen water flux, but still exceeds the cloud ice  
 563 and snow fluxes for updrafts stronger than  $5 \text{ m s}^{-1}$  (see Figure S7d).

### 564 5.3 Categorization of Water Injection by FWP

565 Partitioning the mass fluxes into the three FWP categories described in section 2.5  
 566 further reveals the importance of deep convection in transporting water into the TTL,  
 567 even outside of columns with strong updrafts. Table 2 (see Table S1 for the TWP equiv-  
 568 alent) contains the frequencies of occurrence of each category as well as the category-  
 569 conditional frequencies of vertical velocities above  $\pm 2.5 \text{ m s}^{-1}$  and category-conditional  
 570 average mass fluxes. Category 1 is the least frequent, containing 3.4% or less of all columns  
 571 in the Sahel. Category 1 is slightly more common in the TWP for all models except ICON  
 572 (see Table S1), which is consistent with the more frequent convection over the oceans.  
 573 There is a large intermodel spread in the Category 2 and 3 values and consequently in  
 574 the amount of clear sky. We expect most columns to fall into Category 3 because the  
 575 TTL is dominated by very thin cirrus (e.g., Sassen et al., 2009); this is true in the Sa-  
 576 hel, but Category 2 occurs most often in NICAM and SAM in the TWP. As shown in  
 577 the vertical velocity PDFs (Figure 13b), the overwhelming majority of vertical motion  
 578 in the TTL is very weak, even in areas of deep convection. Vertical velocities exceed  $\pm 2.5 \text{ m s}^{-1}$   
 579 in only 0.2% of Category 1 columns in SAM and less than 0.024% of Category 1 columns  
 580 in NICAM, FV3, and ICON (Table 2). The strong upward mass fluxes in Category 1  
 581 are therefore not restricted to the Category 1 columns having strong updraft speeds.

582 The category-conditional average mass fluxes show the differences in roles played  
 583 by each hydrometeor within the different physical processes in the TTL. Category 1 ac-  
 584 counts for the majority of the total frozen mass flux in both regions even though it con-  
 585 tains a small fraction of columns. As with the integrated values, most of the average Cat-  
 586 egory 1 frozen mass flux comes from graupel flux in NICAM. Graupel flux is slightly less  
 587 important in the TWP, but still accounts for about half of the average frozen flux (see

**Table 2.** Results from Frozen Water Path Categorization in the Sahel

Model	Cat.	Freq.	Freq. of $ w  \geq 2.5 \text{ m s}^{-1}$	Avg. vapor flux ( $\text{kg m}^{-2} \text{ s}^{-1}$ )	Avg. frozen flux ( $\text{kg m}^{-2} \text{ s}^{-1}$ )	Avg. ice flux ( $\text{kg m}^{-2} \text{ s}^{-1}$ )	Avg. snow flux ( $\text{kg m}^{-2} \text{ s}^{-1}$ )	Avg. graupel flux ( $\text{kg m}^{-2} \text{ s}^{-1}$ )
NICAM	1	3.1 %	0.011 %	$7.3 \times 10^{-10}$	$3.1 \times 10^{-6}$	$2.6 \times 10^{-7}$	$4.9 \times 10^{-7}$	$2.4 \times 10^{-6}$
	2	38.8 %	0.018 %	$6.3 \times 10^{-11}$	$-1.2 \times 10^{-8}$	$-1.9 \times 10^{-8}$	$6.8 \times 10^{-9}$	$5.9 \times 10^{-10}$
	3	50.0 %	0.002 %	$2.8 \times 10^{-9}$	$1.9 \times 10^{-10}$	$8.8 \times 10^{-11}$	$1.0 \times 10^{-10}$	$1.2 \times 10^{-14}$
FV3	1	3.4 %	0.024 %	$5.0 \times 10^{-8}$		$1.3 \times 10^{-6}$		
	2	21.4 %	0.033 %	$-1.1 \times 10^{-8}$		$1.9 \times 10^{-8}$		
	3	39.4 %	0.004 %	$5.7 \times 10^{-9}$		$1.8 \times 10^{-9}$		
ICON	1	3.2 %	0.010 %	$3.7 \times 10^{-9}$		$2.4 \times 10^{-7}$		
	2	20.3 %	0.011 %	$-2.9 \times 10^{-9}$		$6.3 \times 10^{-9}$		
	3	26.5 %	0.001 %	$2.1 \times 10^{-9}$		$4.6 \times 10^{-10}$		
SAM	1	3.4 %	0.200 %	$1.1 \times 10^{-8}$		$2.9 \times 10^{-6}$		
	2	32.1 %	0.025 %	$4.1 \times 10^{-9}$		$1.4 \times 10^{-7}$		
	3	35.2 %	0.003 %	$2.1 \times 10^{-8}$		$1.1 \times 10^{-8}$		

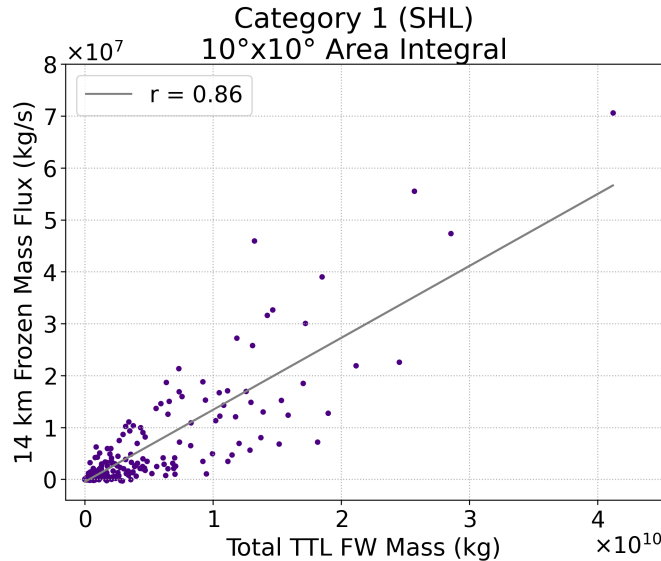
*Note.* The columns list frequency of each frozen water path category, percentage of columns in each category where  $|w| \geq 2.5 \text{ m s}^{-1}$ , and regional- and time-mean mass fluxes for the NFIS models in the Sahel. The mass fluxes are weighted by category frequency.

Table S1). In Category 2, however, most of the frozen flux comes from cloud ice flux. Both the average frozen and cloud ice fluxes are negative, but this does not indicate a net downward flux; these fluxes integrate to nearly zero. The average vapor flux in Category 2 is also much larger than in Category 1, particularly in the TWP (see Table S1), but is still dwarfed by the frozen mass flux. Unsurprisingly, the average frozen mass flux is very small in Category 3 since the thin cirrus contain very little frozen water. Instead, the vapor flux is about 10 times larger than the frozen mass flux within Category 3 and nearly 4 times larger than the Category 1 vapor flux in both regions (Tables 2 and S1).

When the mass fluxes in Categories 2 and 3 are binned by  $w$  as with the total-column fluxes in Figure 13d, the distributions do not reach large  $w$  values and are approximately symmetric around zero (not shown). This symmetry suggests that in areas of both anvil and thin cirrus, the mass fluxes indicate a recycling of air through the 14 km level instead of a systematic upward flux. By extension, this indicates that there is likely much less sedimentation in these areas compared to deep convection. Altogether, the relationships between mass fluxes and FWP categories are surprisingly similar between the Sahel and TWP despite the differences in the characteristics of simulated land and ocean convection described in section 3.

Within Category 1, the  $10^\circ \times 10^\circ$  area-integrated frozen mass flux in NICAM at each time step is strongly correlated with the instantaneous mass of frozen water within the TTL (Figure 14). The frozen mass flux is only weakly related to the total spatial area spanned by Category 1 columns at each time step, with a correlation coefficient half as large as that in Figure 14 (0.42 vs. 0.86). Therefore, a larger area of deep convection does not necessarily bring more frozen water into the TTL. The relationship in Figure 14 suggests that there is a regional-mean time scale of about 722 seconds (the reciprocal of the slope of the regression line) in the Sahel for the frozen water injected into the TTL to fall out or evolve into thinner cirrus (i.e., Categories 2 and 3). The same relationship is present in the TWP, but the time scale is longer at 1575 seconds (Figure S8). Compared to the Sahel, the weaker updrafts in the TWP tend to loft smaller ice particles that will take longer to sediment out of the TTL. Since NICAM has much more cloud ice in the TTL in both regions than FV3, ICON, or SAM, it is unclear if this ice removal timescale will quantitatively hold for the other models.

In NICAM, deep convection injects frozen water and vapor at 14 km and deposits it throughout the depth of the TTL. Figure 15 shows vertical profiles of the average frozen water and vapor mass fluxes (normalized by the 38-day average precipitation rate in the Sahel) as well as the largest 0.1% of vertical velocities within the updrafts or downdrafts (see Figure S9 for the TWP equivalent, normalized by the TWP average precipitation



**Figure 14.** Correlations between the area-integrated Category 1 frozen mass flux at 14 km and the total mass of frozen water (FW) in the TTL in Category 1 for NICAM in the Sahel. Each point represents one instantaneous time step over days 3–40 of the model run with variables integrated over the  $10^\circ \times 10^\circ$  Sahel region. The least-squares regression line is shown in gray with the correlation coefficient ( $r$ ) in the legend.

rate). These profiles are for all columns, but as previously discussed, the Category 1 frozen mass flux makes up nearly all of the total frozen mass flux. In both regions, the frozen mass flux dominates throughout the lower TTL up to about 16.5 km, at which point it is overtaken by the vapor flux. This pattern agrees qualitatively with Bolot and Fueglistaler (2021), who found that deep convection is more important for moisture transport than large-scale advection (i.e., our Category 3 mass fluxes) below the cold point ( $\sim 16\text{--}17$  km). However, the frozen mass flux values in NICAM are larger by a factor of  $\sim 100$  in both regions than the observationally-based, tropics-wide estimates from Bolot and Fueglistaler (2021). We normalize the estimates of ice flux from Figure 3 in Bolot and Fueglistaler (2021) by the area of their  $30^\circ\text{S}\text{--}30^\circ\text{N}$  domain as well as the 38-day average Sahel or TWP precipitation rate. These estimates are then plotted alongside the NICAM values in Figures 15 and S9.

#### 5.4 Frozen Water Flux into the TTL in Other Models

We cannot generalize the mass flux results in NICAM to the other models. The regional- and time-mean cloud ice mass fluxes at 14 km vary by a factor of 10 in the NFIS models within both regions (Table 2). We also expect the specific values of 14 km frozen and vapor mass fluxes to differ significantly between the NFIS models based on the vertical velocities, FWC, and WV. Although the 14 km IWC is very similar between models in the bins above  $\pm 5 \text{ m s}^{-1}$  (Figure 13a), there are substantial differences in the relative proportions of cloud ice, snow, and graupel (Figure 11). Thus, the 14 km FWC will likely vary more than the 14 km IWC. Likewise, FV3 and ICON both have very different frequencies of updrafts exceeding  $10 \text{ m s}^{-1}$  than NICAM (Figure 13), which determine the most intense mass flux values in those models.

Regardless of the anticipated differences in the amounts of mass injected into the TTL, we still expect deep convection to be the most important process in supplying wa-

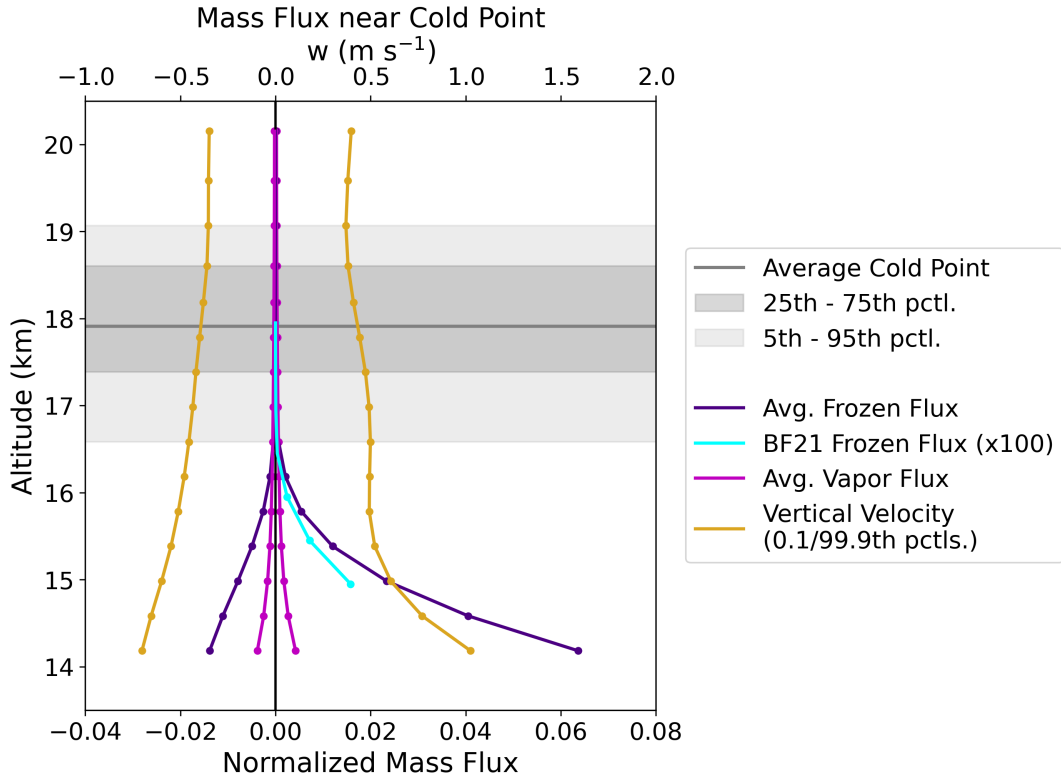


**Figure 15.** Vertical profiles of normalized frozen water (purple lines) and vapor mass fluxes (dark pink lines) for NICAM in the Sahel as well as the normalized estimates of frozen mass flux from Bolot and Fueglistaler (2021) times 100 (BF21; cyan line). The mass fluxes for NICAM are split between updrafts and downdrafts, averaged over the  $10^\circ \times 10^\circ$  region and time, and weighted by the relative frequency of the updrafts or downdrafts. The gold lines show the 0.1th and 99.9th percentiles of vertical velocity. The average cold point height is shown in the solid gray line while the 5th–95th (25th–75th) percentiles are shaded in light (dark) gray. All percentiles are taken over the  $10^\circ \times 10^\circ$  Sahel region and days 3–40 of the model run.

649 ter into the TTL. In all of the NFIS models, the concentration of cloud ice over deep con-  
 650vection is very high (see section 5.1). This proportion will only increase once graupel and  
 651snow are considered because these hydrometeors make up 50–87% of the total integrated  
 652FWP in FV3, ICON, and SAM (Figure 11). Since the 14 km WV in FV3, ICON, and  
 653SAM is similar to that in NICAM (Figure 13c), we can assume that the frozen mass flux  
 654will be much larger than the vapor flux in the other models. Nevertheless, we cannot draw  
 655any definitive conclusions about the frozen mass flux in other models without access to  
 656the 3D profiles of snow and graupel in FV3, ICON, or SAM.

## 6 Summary and Discussion

In this paper, we have used satellite and reanalysis data to evaluate the simulation of convectively generated cirrus in GSRMs from the DYAMOND project. These GSRMs all have horizontal grid spacing below 5 km, which permits explicit convection (Stevens et al., 2019). We focused on four models which archived cloud ice at the full native grid resolution: NICAM, FV3, ICON, and SAM. We analyzed two representative  $10^\circ \times 10^\circ$

663 latitude-longitude regions, one over the Sahel in western Africa and one over the trop-  
 664 ical West Pacific.

665 Before analyzing how convection generates tropical cirrus in the DYAMOND GSRMs,  
 666 we first assessed how well the GSRMs reproduce deep convection. As a group, the DYAMOND  
 667 GSRMs simulate deep convective precipitation, its organization, and its diurnal cycle fairly  
 668 well over both the land and ocean regions, though intermodel scatter is large. In contrast,  
 669 GCMs struggle with these tasks. The GSRM-simulated convective updraft and downdraft  
 670 strengths have qualitatively similar frequency distributions. All the GSRMs produce  
 671 frequent overshooting convection that reaches the TTL; in most models, convective  
 672 updrafts occasionally penetrate the cold point tropopause. In all GSRMs and both regions,  
 673 the time-mean relative humidity with respect to ice is  $\sim$ 70–90% in the TTL.  
 674

675 For the convective cloud properties (water content vertical profiles and the cloud  
 676 microphysics, including partitioning between cloud liquid, ice, snow, and graupel) and  
 677 the convective injection of frozen water into the TTL, differences between GSRMs exceed  
 678 differences between land and ocean regions, consistent with the findings of Turbeville  
 679 et al. (2021) in Part II of this study. In NICAM in both regions, the most intense con-  
 680 vective updrafts inject nearly all of the incoming frozen water into the TTL. We presume  
 681 that most of this injected ice sediments out of the TTL near the deep convection, although  
 682 we did not have the necessary information to be sure. We found that across the mod-  
 683 els, the mass of frozen water within the TTL correlates with the deep convective frozen  
 684 mass flux into the TTL; their ratio suggests an ice residence time of about ten to thirty  
 685 minutes.

686 Our analysis was limited by the output variables available for most of the DYAMOND  
 687 GSRMs. Having the 3D profiles of snow and graupel water contents would allow for evalua-  
 688 tion of intermodel differences in the frozen mass fluxes and TTL FWC. Because cloud  
 689 microphysics parameterizations are a major source of intermodel differences, saving the full  
 690 hydrometeor profiles should be prioritized in future GSRM simulations.

691 We have focused on how water vapor and frozen water reach the TTL. What hap-  
 692 pens to the injected mass afterward is also critical to understanding the relationship be-  
 693 tween TTL cirrus and deep convection. In Part II of this paper, Turbeville et al. (2021)  
 694 explore the full distribution of tropical cirrus in the DYAMOND GSRMs, including tran-  
 695 sitions between the three FWP categories introduced here. The models simulate the ob-  
 696 served transition between deep convection and thin cirrus, though with clear model-specific  
 697 biases (Turbeville et al., 2021). That analysis could not address two scientifically impor-  
 698 tant questions: how quickly air moves from Category 1 (deep convection) to Category  
 699 2 (thick cirrus) and how much frozen water is transported between categories vs. how  
 700 much sediments out.

701 Despite their present limitations, GSRMs are a promising complement to climate  
 702 models for the simulation of cirrus initiated by deep convection, including within the TTL.  
 703 This study shows that subgrid processes drive the substantial variation between mod-  
 704 els. Specifically, the model microphysics and, to a lesser extent, the dynamical flow solver  
 705 may both be important. We suspect that improved microphysics would more readily ad-  
 706 vance the simulation of tropical cirrus than higher spatial resolutions. The sub-5 km hor-  
 707 izontal and 200–500 m vertical grid spacings seem sufficient to simulate cirrus and may  
 708 capture gravity wave activity around deep convection that is thought to be important  
 709 for TTL cirrus, though this has not been clearly shown. Radiatively-driven circulations  
 710 within TTL cirrus (Durran et al., 2009) would require finer grids to explicitly resolve;  
 711 whether subgrid turbulence parameterizations can represent this process adequately re-  
 712 mains to be seen. Overall, this work has demonstrated that GSRMs model deep convec-  
 713 tion realistically enough to form a good foundation for simulating convectively gener-  
 714 ated cirrus and their impacts on the TTL, climate more broadly, and climate change.

715 Careful observationally-based improvements of GSRMs are needed to fully realize this  
 716 potential.

### 717 Acknowledgments

718 We thank Adam Sokol and Blaž Gasparini for their help with obtaining and analyzing  
 719 the DARDAR and CCCM data. This material is based upon work supported by the Na-  
 720 tional Science Foundation through the Partnerships in International Research and Ed-  
 721 ucation program under grant number OISE-1743753. DYAMOND data management was  
 722 provided by the German Climate Computing Center (DKRZ) and supported through  
 723 the projects ESiWACE and ESiWACE2, which have received funding from the European  
 724 Union's Horizon 2020 research and innovation program under grant agreements No. 675191  
 725 and 823988. DARDAR data were obtained from the ICARE Data and Services Center  
 726 (<http://www.icare.univ-lille1.fr/projects/dardar>). The TRMM 3B42 data were  
 727 obtained from <https://doi.org/10.5067/TRMM/TMPA/3H/7>. The satellite data from the  
 728 A-Train Integrated CALIPSO, CloudSat, CERES, and MODIS Merged Product Release  
 729 B1 (CCCM) were obtained from [https://doi.org/10.5067/AQUA/CERES/NEWS\\_CCCM-FM3-MODIS-CAL-CS\\_L2.RELB1](https://doi.org/10.5067/AQUA/CERES/NEWS_CCCM-FM3-MODIS-CAL-CS_L2.RELB1). The ERA5 hourly data on pressure levels were obtained  
 730 from the Copernicus Climate Data Store (<https://doi.org/10.24381/cds.bd0915c6>).  
 731

### 732 References

- 733 Arteta, J., Marecal, V., & Riviere, E. D. (2009). Regional modelling of tracer  
 734 transport by tropical convection – Part 1: Sensitivity to convection parameteri-  
 735 zation. *Atmos. Chem. Phys.*, 20. doi: 10.5194/acp-9-7081-2009
- 736 Avery, M., Winker, D., Heymsfield, A., Vaughan, M., Young, S., Hu, Y., & Trepte,  
 737 C. (2012). Cloud ice water content retrieved from the CALIOP space-based li-  
 738 dar: CALIOP ICE WATER CONTENT. *Geophysical Research Letters*, 39(5).  
 739 doi: 10.1029/2011GL050545
- 740 Bechtold, P., Chaboureau, J.-P., Beljaars, A., Betts, A., Köhler, M., Miller, M., &  
 741 Redelsperger, J.-L. (2004). The simulation of the diurnal cycle of convective  
 742 precipitation over land in a global model. *Quarterly Journal of the Royal  
 743 Meteorological Society*, 130(604), 3119–3137. doi: 10.1256/qj.03.103
- 744 Berthou, S., Rowell, D. P., Kendon, E. J., Roberts, M. J., Stratton, R. A., Crook,  
 745 J. A., & Wilcox, C. (2019). Improved climatological precipitation character-  
 746 istics over West Africa at convection-permitting scales. *Climate Dynamics*,  
 747 53(3-4), 1991–2011. doi: 10.1007/s00382-019-04759-4
- 748 Bolot, M., & Fueglistaler, S. (2021). Tropical Water Fluxes Dominated by Deep  
 749 Convection Up to Near Tropopause Levels. *Geophysical Research Letters*,  
 750 48(4). doi: 10.1029/2020GL091471
- 751 Bousquet, O., & Chong, M. (2000). The oceanic mesoscale convective system and  
 752 associated mesovortex observed 12 December 1992 during TOGA-COARE.  
 753 *Quarterly Journal of the Royal Meteorological Society*, 126(562), 189–211. doi:  
 754 10.1002/qj.49712656210
- 755 Chao, W. C. (2013). Catastrophe-Concept-Based Cumulus Parameterization: Cor-  
 756 rection of Systematic Errors in the Precipitation Diurnal Cycle over Land  
 757 in a GCM. *Journal of the Atmospheric Sciences*, 70(11), 3599–3614. doi:  
 758 10.1175/JAS-D-13-022.1
- 759 Delanoë, J., & Hogan, R. J. (2008). A variational scheme for retrieving ice cloud  
 760 properties from combined radar, lidar, and infrared radiometer. *Journal of  
 761 Geophysical Research*, 113(D7), D07204. doi: 10.1029/2007JD009000
- 762 Delanoë, J., & Hogan, R. J. (2010). Combined CloudSat-CALIPSO-MODIS re-  
 763 trievals of the properties of ice clouds. *Journal of Geophysical Research*, 115,  
 764 D00H29. doi: 10.1029/2009JD012346
- 765 Deng, M., Mace, G. G., Wang, Z., & Lawson, R. P. (2013). Evaluation of Several

- 766 A-Train Ice Cloud Retrieval Products with In Situ Measurements Collected  
 767 during the SPARTICUS Campaign. *Journal of Applied Meteorology and Cli-*  
 768 *matology*, 52(4), 1014–1030. doi: 10.1175/JAMC-D-12-054.1
- 769 Dessler, A. E., Palm, S. P., Hart, W. D., & Spinhirne, J. D. (2006). Tropopause-  
 770 level thin cirrus coverage revealed by ICESat/Geoscience Laser Altimeter  
 771 System. *Journal of Geophysical Research*, 111(D8), D08203. doi:  
 772 10.1029/2005JD006586
- 773 Duda, J. D., & Gallus, W. A. (2013). The Impact of Large-Scale Forcing on Skill  
 774 of Simulated Convective Initiation and Upscale Evolution with Convection-  
 775 Allowing Grid Spacings in the WRF\*. *Weather and Forecasting*, 28(4), 994–  
 776 1018. doi: 10.1175/WAF-D-13-00005.1
- 777 Durran, D. R., Dinh, T., Ammerman, M., & Ackerman, T. (2009). The Mesoscale  
 778 Dynamics of Thin Tropical Tropopause Cirrus. *Journal of the Atmospheric  
 779 Sciences*, 66(9), 2859–2873. doi: 10.1175/2009JAS3046.1
- 780 Fierli, F., Orlandi, E., Law, K. S., Cagnazzo, C., Cairo, F., Schiller, C., ... Volk,  
 781 C. M. (2011). Impact of deep convection in the tropical tropopause layer  
 782 in West Africa: in-situ observations and mesoscale modelling. *Atmospheric  
 783 Chemistry and Physics*, 11(1), 201–214. doi: 10.5194/acp-11-201-2011
- 784 Fueglistaler, S., Dessler, A. E., Dunkerton, T. J., Folkins, I., Fu, Q., & Mote, P. W.  
 785 (2009). Tropical tropopause layer. *Reviews of Geophysics*, 47(1). (Publisher:  
 786 John Wiley & Sons, Ltd) doi: 10.1029/2008RG000267
- 787 Futyan, J. M., Russell, J. E., & Harries, J. E. (2004). Cloud Radiative Forcing  
 788 in Pacific, African, and Atlantic Tropical Convective Regions. *JOURNAL OF  
 789 CLIMATE*, 17, 11. doi: 10.1175/1520-0442(2004)017<3192:CRFIPA>2.0.CO;2
- 790 Haladay, T., & Stephens, G. (2009). Characteristics of tropical thin cirrus clouds de-  
 791 duced from joint CloudSat and CALIPSO observations. *Journal of Geophysical  
 792 Research*, 114, D00A25. doi: 10.1029/2008JD010675
- 793 Hersbach, H., Bell, B., Berrisford, P., Hirahara, S., Horányi, A., Muñoz-Sabater, J.,  
 794 ... Thépaut, J. (2020). The ERA5 global reanalysis. *Quarterly Journal of the  
 795 Royal Meteorological Society*, 146(730), 1999–2049. doi: 10.1002/qj.3803
- 796 Huffman, G. J., Adler, R. F., Bolvin, D. T., & Nelkin, E. J. (2010). The TRMM  
 797 Multi-Satellite Precipitation Analysis (TMPA). In M. Gebremichael & F. Hos-  
 798 sain (Eds.), *Satellite Rainfall Applications for Surface Hydrology* (pp. 3–22).  
 799 Dordrecht: Springer Netherlands. doi: 10.1007/978-90-481-2915-7\_1
- 800 Huffman, G. J., & Bolvin, D. T. (2018). *TRMM and Other Data Precipi-*  
 801 *tation Set Documentation*. NASA/GSFC. Retrieved 2021-02-19, from  
 802 [https://docserver.gesdisc.eosdis.nasa.gov/public/project/GPM/3B42\\_3B43\\_doc\\_V7.pdf](https://docserver.gesdisc.eosdis.nasa.gov/public/project/GPM/3B42_3B43_doc_V7.pdf)
- 803 Huffman, G. J., Bolvin, D. T., Nelkin, E. J., Wolff, D. B., Adler, R. F., Gu, G.,  
 804 ... Stocker, E. F. (2007). The TRMM Multisatellite Precipitation Anal-  
 805 ysis (TMPA): Quasi-Global, Multiyear, Combined-Sensor Precipitation Es-  
 806 timates at Fine Scales. *Journal of Hydrometeorology*, 8(1), 38–55. doi:  
 807 10.1175/JHM560.1
- 808 Inoue, T., Satoh, M., Miura, H., & Mapes, B. (2008). Characteristics of Cloud Size  
 809 of Deep Convection Simulated by a Global Cloud Resolving Model over the  
 810 Western Tropical Pacific. *Journal of the Meteorological Society of Japan*, 86A,  
 811 1–15. doi: 10.2151/jmsj.86A.1
- 812 Jensen, E. J., Toon, O. B., Pfister, L., & Selkirk, H. B. (1996a). Dehydration of the  
 813 upper troposphere and lower stratosphere by subvisible cirrus clouds near the  
 814 tropical tropopause. *Geophysical Research Letters*, 23(8), 825–828. (Publisher:  
 815 John Wiley & Sons, Ltd) doi: 10.1029/96GL00722
- 816 Jensen, E. J., Toon, O. B., Selkirk, H. B., Spinhirne, J. D., & Schoeberl, M. R.  
 817 (1996b). On the formation and persistence of subvisible cirrus clouds near the  
 818 tropical tropopause. *Journal of Geophysical Research: Atmospheres*, 101(D16),  
 819 21361–21375. doi: 10.1029/95JD03575

- Jensen, E. J., Ueyama, R., Pfister, L., Bui, T. V., Alexander, M. J., Podglajen, A., ... Schoeberl, M. R. (2016). High-frequency gravity waves and homogeneous ice nucleation in tropical tropopause layer cirrus: WAVES AND ICE NUCLEATION. *Geophysical Research Letters*, 43(12), 6629–6635. doi: 10.1002/2016GL069426
- Kato, S., Rose, F. G., Sun-Mack, S., Miller, W. F., Chen, Y., Rutan, D. A., ... Collins, W. D. (2011). Improvements of top-of-atmosphere and surface irradiance computations with CALIPSO-, CloudSat-, and MODIS-derived cloud and aerosol properties. *Journal of Geophysical Research*, 116(D19), D19209. doi: 10.1029/2011JD016050
- Kato, S., Sun-Mack, S., Miller, W. F., Rose, F. G., Chen, Y., Minnis, P., & Wielicki, B. A. (2010). Relationships among cloud occurrence frequency, overlap, and effective thickness derived from CALIPSO and CloudSat merged cloud vertical profiles. *Journal of Geophysical Research*, 115, D00H28. doi: 10.1029/2009JD012277
- Khairoutdinov, M., Randall, D., & DeMott, C. (2005). Simulations of the Atmospheric General Circulation Using a Cloud-Resolving Model as a Superparameterization of Physical Processes. *Journal of the Atmospheric Sciences*, 62(7), 2136–2154. doi: 10.1175/JAS3453.1
- Krämer, M., Rolf, C., Luebke, A., Afchine, A., Spelten, N., Costa, A., ... Avalone, L. (2016). A microphysics guide to cirrus clouds – Part 1: Cirrus types. *Atmospheric Chemistry and Physics*, 16(5), 3463–3483. doi: 10.5194/acp-16-3463-2016
- Lee, J., Yang, P., Dessler, A. E., Gao, B.-C., & Platnick, S. (2009). Distribution and Radiative Forcing of Tropical Thin Cirrus Clouds. *Journal of the Atmospheric Sciences*, 66(12), 3721–3731. doi: 10.1175/2009JAS3183.1
- Liu, C., & Zipser, E. J. (2005). Global distribution of convection penetrating the tropical tropopause. *Journal of Geophysical Research*, 110(D23), D23104. doi: 10.1029/2005JD006063
- Liu, C., Zipser, E. J., & Nesbitt, S. W. (2007). Global Distribution of Tropical Deep Convection: Different Perspectives from TRMM Infrared and Radar Data. *Journal of Climate*, 20(3), 489–503. doi: 10.1175/JCLI4023.1
- Long, C. N., Mather, J. H., & Ackerman, T. P. (2016). The ARM Tropical Western Pacific (TWP) Sites. *Meteorological Monographs*, 57, 7.1–7.14. doi: 10.1175/AMSMONOGRAPH-D-15-0024.1
- Luo, Z., & Rossow, W. B. (2004). Characterizing Tropical Cirrus Life Cycle, Evolution, and Interaction with Upper-Tropospheric Water Vapor Using Lagrangian Trajectory Analysis of Satellite Observations. *Journal of Climate*, 17(23), 4541–4563. doi: 10.1175/3222.1
- Mace, G. G., Deng, M., Soden, B., & Zipser, E. (2006). Association of Tropical Cirrus in the 10–15-km Layer with Deep Convective Sources: An Observational Study Combining Millimeter Radar Data and Satellite-Derived Trajectories. *Journal of the Atmospheric Sciences*, 63(2), 480–503. doi: 10.1175/JAS3627.1
- Massie, S., Gettelman, A., Randel, W., & Baumgardner, D. (2002). Distribution of tropical cirrus in relation to convection: DISTRIBUTION OF TROPICAL CIRRUS. *Journal of Geophysical Research: Atmospheres*, 107(D21), AAC 19–1–AAC 19–16. doi: 10.1029/2001JD001293
- Murphy, D. M., & Koop, T. (2005). Review of the vapour pressures of ice and supercooled water for atmospheric applications. *Quarterly Journal of the Royal Meteorological Society*, 131(608), 1539–1565. doi: 10.1256/qj.04.94
- Nesbitt, S. W., & Zipser, E. J. (2003). The Diurnal Cycle of Rainfall and Convective Intensity according to Three Years of TRMM Measurements. *JOURNAL OF CLIMATE*, 16, 20. doi: 10.1175/1520-0442(2003)016<1456:TDCORA>2.0.CO;2

- 876 Redelsperger, J.-L., Diongue, A., Diedhiou, A., Ceron, J.-P., Diop, M., Gueremy,  
 877 J.-F., & Lafore, J.-P. (2002). Multi-scale description of a Sahelian syn-  
 878 optic weather system representative of the West African monsoon. *Quar-*  
 879 *terly Journal of the Royal Meteorological Society*, 128(582), 1229–1257. doi:  
 880 10.1256/003590002320373274
- 881 Redelsperger, J.-L., & Lafore, J.-P. (1988). A Three-Dimensional Simulation  
 882 of a Tropical Squall Line: Convective Organization and Thermodynamic  
 883 Vertical Transport. *Journal of Atmospheric Sciences*, 45(8), 1334 – 1356.  
 884 (Place: Boston MA, USA Publisher: American Meteorological Society) doi:  
 885 10.1175/1520-0469(1988)045<1334:ATDSOA>2.0.CO;2
- 886 Sassen, K., Wang, Z., & Liu, D. (2009). Cirrus clouds and deep convection in  
 887 the tropics: Insights from CALIPSO and CloudSat. *Journal of Geophysical*  
 888 *Research*, 114, D00H06. doi: 10.1029/2009JD011916
- 889 Schoeberl, M. R., Jensen, E. J., Pfister, L., Ueyama, R., Avery, M., & Dessler, A. E.  
 890 (2018). Convective Hydration of the Upper Troposphere and Lower Strato-  
 891 sphere. *Journal of Geophysical Research: Atmospheres*, 123(9), 4583–4593.  
 892 doi: 10.1029/2018JD028286
- 893 Slingo, A., Bharmal, N. A., Robinson, G. J., Settle, J. J., Allan, R. P., White, H. E.,  
 894 ... Miller, M. (2008). Overview of observations from the RADAGAST experi-  
 895 ment in Niamey, Niger: Meteorology and thermodynamic variables. *Journal of*  
 896 *Geophysical Research*, 113, D00E01. doi: 10.1029/2008JD009909
- 897 Sokol, A. B., & Hartmann, D. L. (2020). Tropical Anvil Clouds: Radiative Driv-  
 898 ing Toward a Preferred State. *Journal of Geophysical Research: Atmospheres*,  
 899 125(21). doi: 10.1029/2020JD033107
- 900 Solomon, S., Rosenlof, K. H., Portmann, R. W., Daniel, J. S., Davis, S. M., Sanford,  
 901 T. J., & Plattner, G.-K. (2010). Contributions of Stratospheric Water Va-  
 902 por to Decadal Changes in the Rate of Global Warming. *Science*, 327(5970),  
 903 1219–1223. doi: 10.1126/science.1182488
- 904 Stephens, G. L., Vane, D. G., Boain, R. J., Mace, G. G., Sassen, K., Wang, Z., ...  
 905 the CloudSat Science Team (2002). THE CLOUDSAT MISSION AND THE  
 906 A-TRAIN: A New Dimension of Space-Based Observations of Clouds and Pre-  
 907 cipitation. *Bulletin of the American Meteorological Society*, 83(12), 1771–1790.  
 908 doi: 10.1175/BAMS-83-12-1771
- 909 Stevens, B., Satoh, M., Auger, L., Biercamp, J., Bretherton, C. S., Chen, X., ...  
 910 Zhou, L. (2019). DYAMOND: the DYnamics of the Atmospheric general circu-  
 911 lation Modeled On Non-hydrostatic Domains. *Progress in Earth and Planetary*  
 912 *Science*, 6(1), 61. doi: 10.1186/s40645-019-0304-z
- 913 Turbeville, S. M., Nugent, J. M., Ackerman, T. P., Bretherton, C. S., & Blossey,  
 914 P. N. (2021). *Tropical cirrus in global storm-resolving models. Part II:*  
 915 *Cirrus Life Cycle and Top-of-Atmosphere Radiative Fluxes.* (Unpublished  
 916 manuscript)
- 917 Ueyama, R., Jensen, E. J., & Pfister, L. (2018). Convective Influence on the Hu-  
 918 midity and Clouds in the Tropical Tropopause Layer During Boreal Summer.  
 919 *Journal of Geophysical Research: Atmospheres*. doi: 10.1029/2018JD028674
- 920 Virtz, K. S., & Houze, R. A. (2015). Clouds and Water Vapor in the Tropical  
 921 Tropopause Transition Layer over Mesoscale Convective Systems. *Journal of*  
 922 *the Atmospheric Sciences*, 72(12), 4739–4753. doi: 10.1175/JAS-D-15-0122.1
- 923 Yang, G.-Y., & Slingo, J. (2001). The Diurnal Cycle in the Tropics. *MONTHLY*  
 924 *WEATHER REVIEW*, 129, 18. doi: 10.1175/1520-0493(2001)129<0784:  
 925 TDCITT>2.0.CO;2
- 926 Zipser, E. J., Cecil, D. J., Liu, C., Nesbitt, S. W., & Yorty, D. P. (2006). WHERE  
 927 ARE THE MOST INTENSE THUNDERSTORMS ON EARTH? *Bulletin of*  
 928 *the American Meteorological Society*, 87(8), 1057–1072. doi: 10.1175/BAMS-87  
 929 -8-1057

# Supporting Information for “Tropical Cirrus in Global Storm-Resolving Models. Part I: Role of Deep Convection”

J. M. Nugent<sup>1</sup>, S. M. Turbeville<sup>1</sup>, C. S. Bretherton<sup>1,2</sup>, P. N. Blossey<sup>1</sup>, and

T. P. Ackerman<sup>1,3</sup>

<sup>1</sup>Department of Atmospheric Sciences, University of Washington, Seattle, WA

<sup>2</sup>Vulcan, Inc., Seattle, WA

<sup>3</sup>Joint Institute for the Study of the Atmosphere and Ocean, University of Washington, Seattle, WA

## Contents of this file

1. Figures S1 to S9

2. Table S1

**Introduction** This supplement includes the figures and table for the tropical West Pacific (TWP) region (Figures S1–S3, S7–S9; Table S1) that correspond to the Sahel-only figures and table in the main article. The time series of outgoing longwave radiation, precipitation rate, total-column and tropical tropopause layer ice water paths, and fractional areas of each category for NICAM, ICON, and SAM (Figures S4–S6) are also included; these time series are only shown for FV3 in the main article. Descriptions of all supplementary figures and the supplementary table are included in the main article.

---

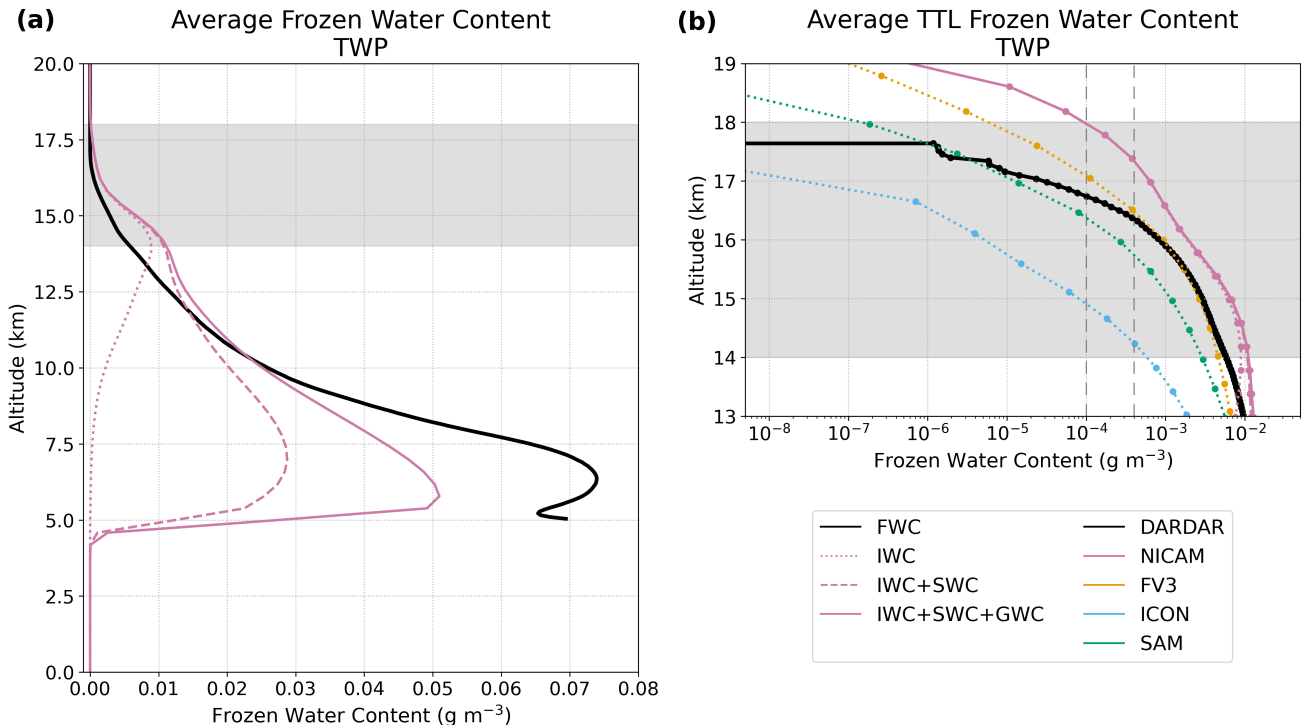


**Figure S1.** Same as Figure 9 in the paper, but for the TWP. The TWP region experienced anomalously high precipitation in 2009 when DARDAR measurements were taken, so the apparent underestimation of peak FWC in NICAM is likely exaggerated here.

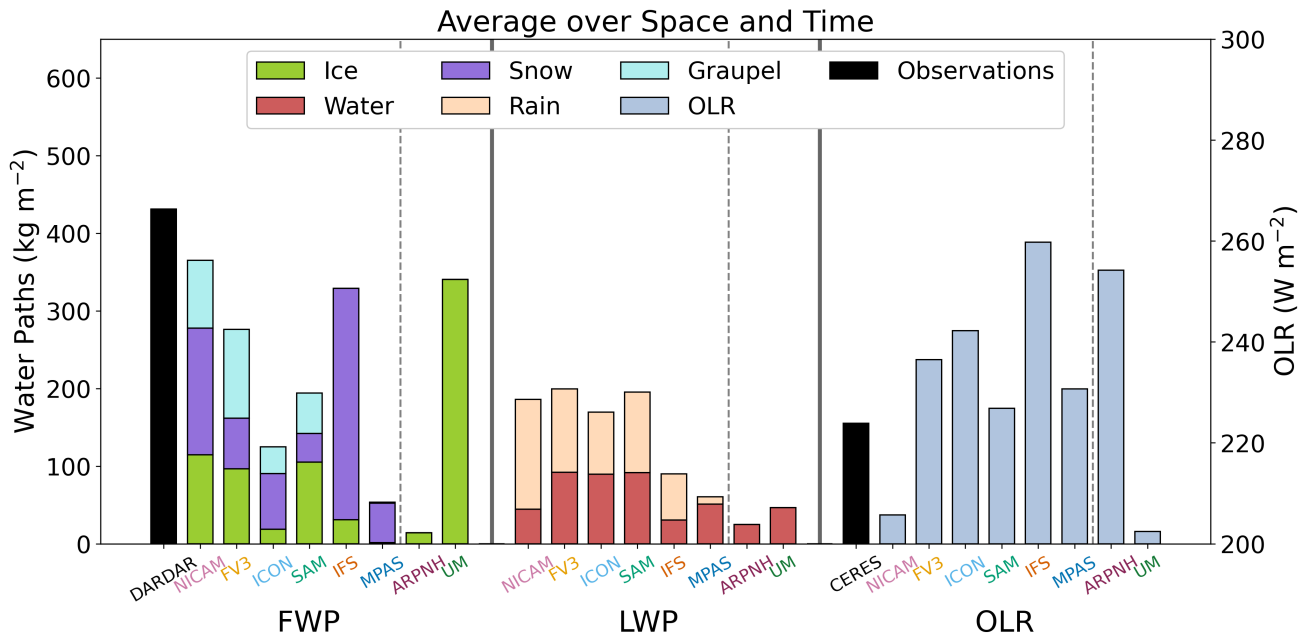


**Figure S2.** Same as Figure 10 in the paper, but for the TWP.

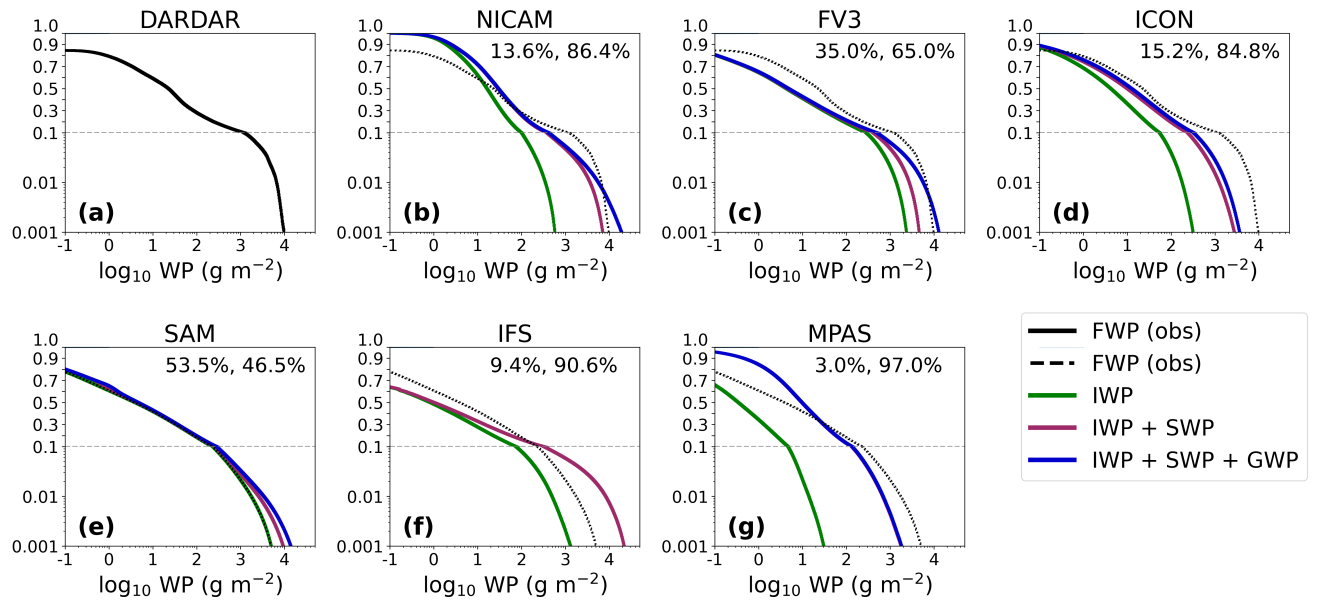


**Figure S3.** Same as Figure 11 in the paper, but for the TWP.

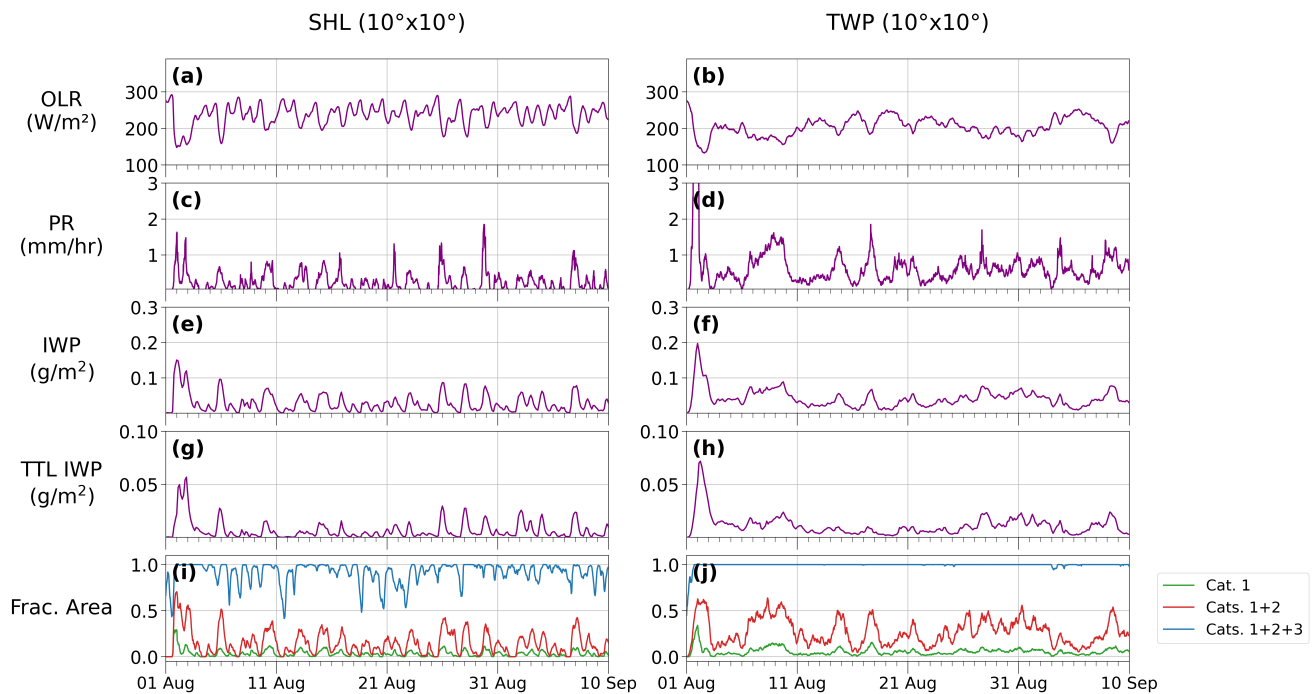


**Figure S4.** Same as Figure 12 in the paper, but for NICAM.

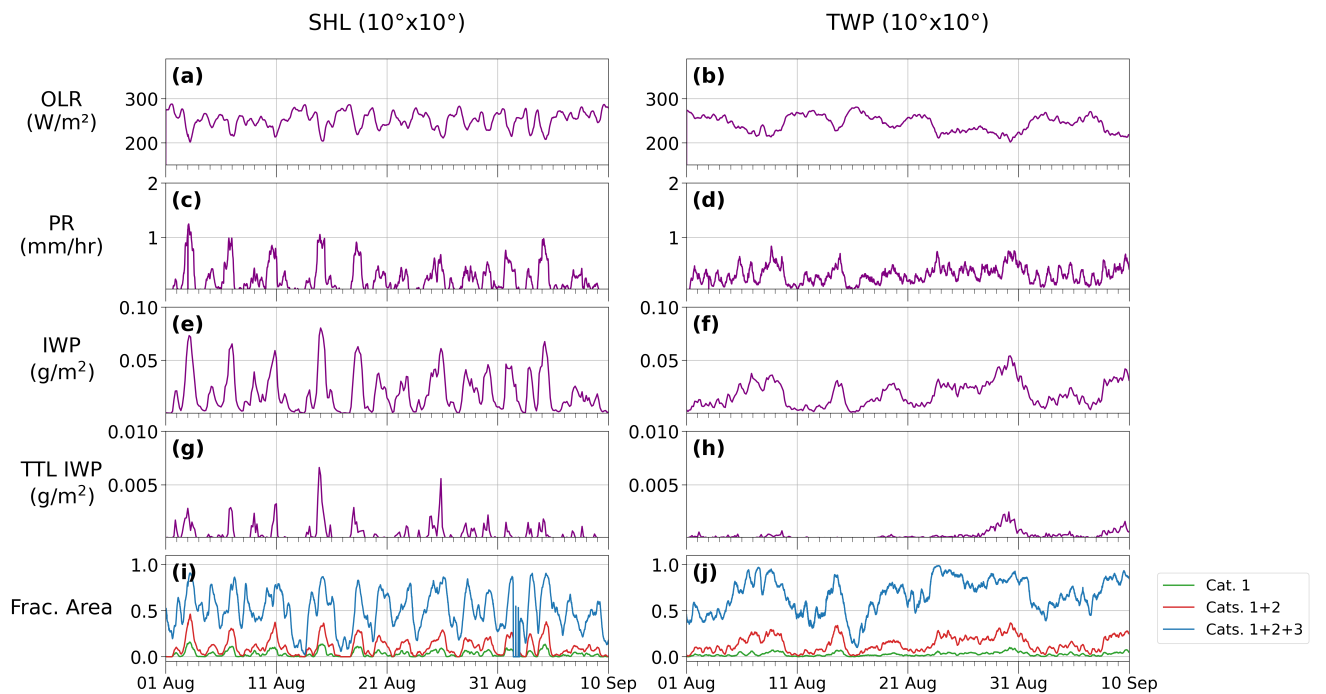


**Figure S5.** Same as Figure 12 in the paper, but for ICON.

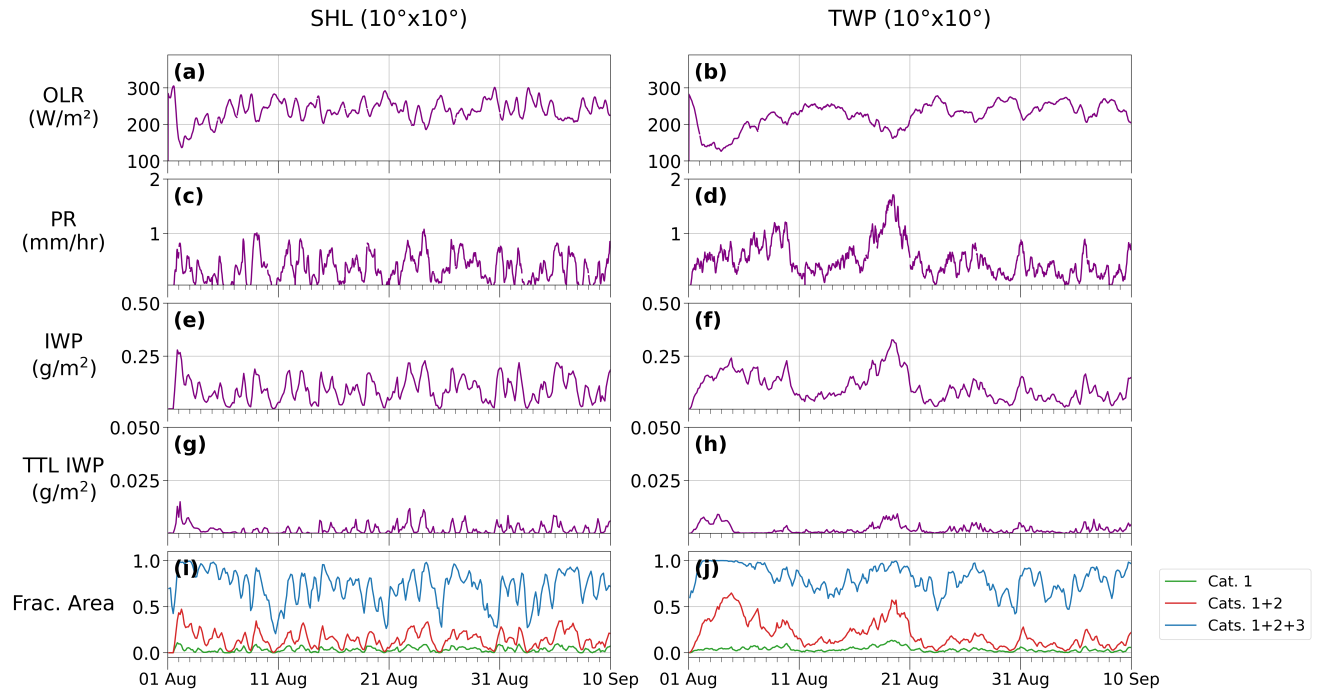


**Figure S6.** Same as Figure 12 in the paper, but for SAM.

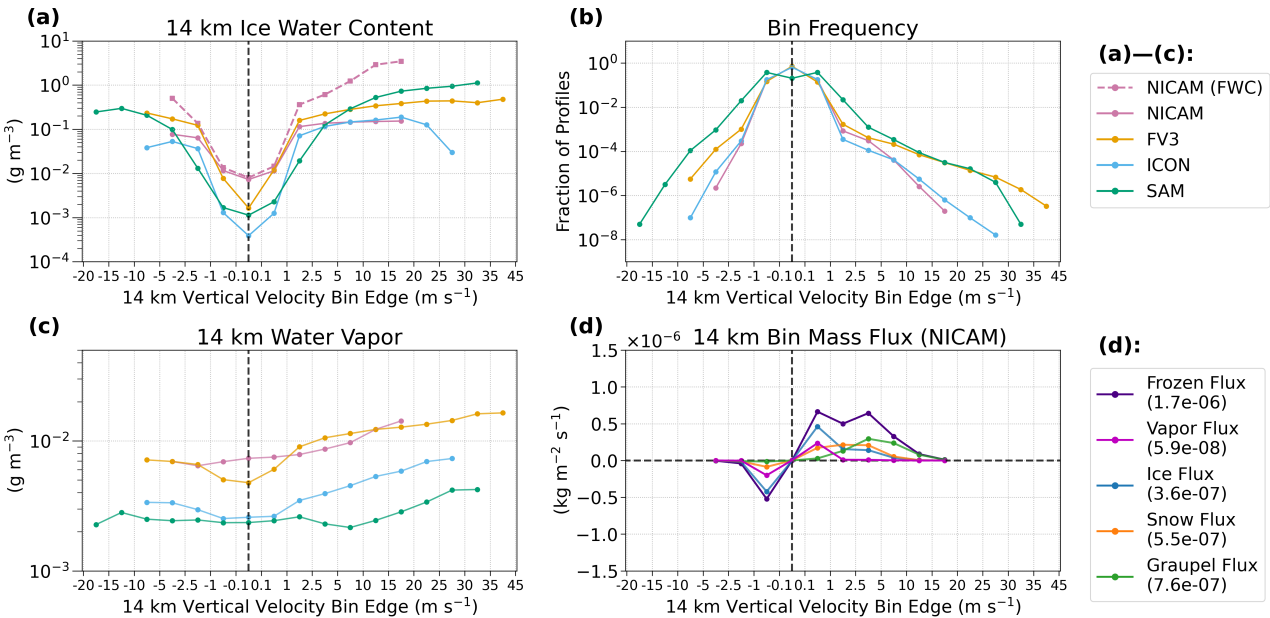


**Figure S7.** Same as Figure 13 in the paper, but for the TWP.

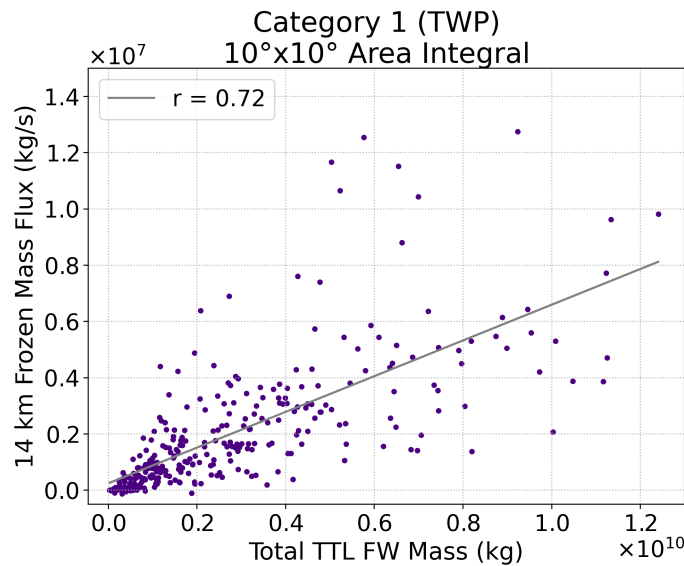


**Figure S8.** Same as Figure 14 in the paper, but for the TWP.

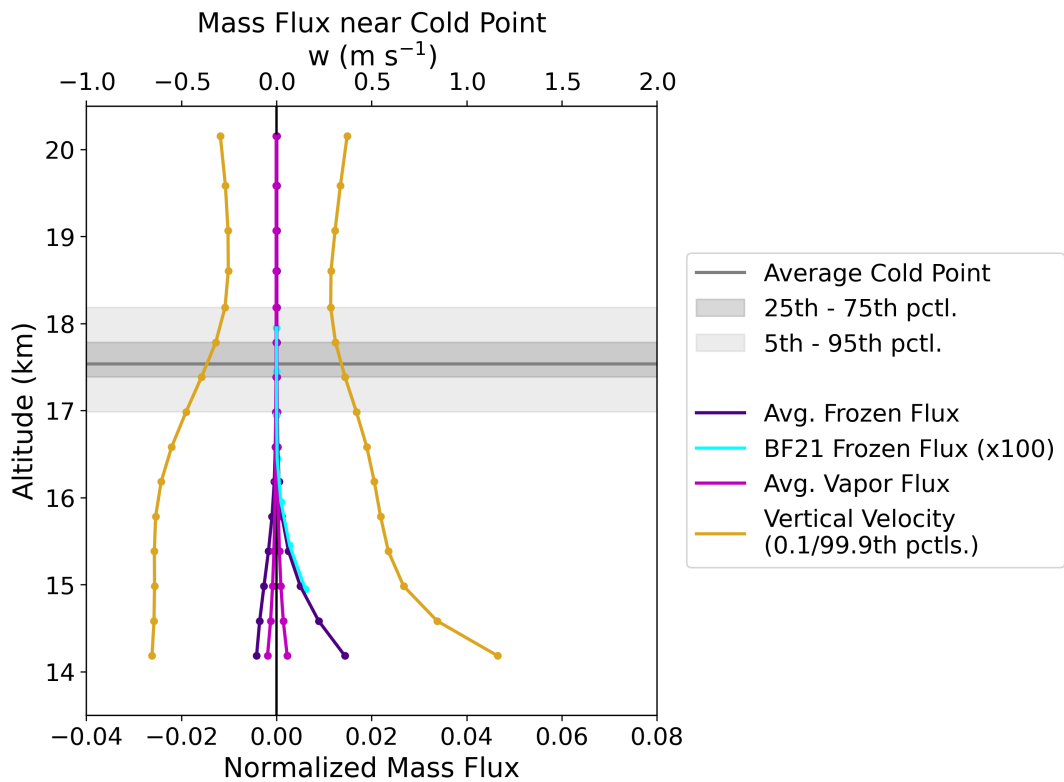


**Figure S9.** Same as Figure 15 in the paper, but for the TWP.

**Table S1.** Results from Frozen Water Path Categorization in the TWP

Model	Cat.	Freq.	Freq. of $ w  \geq 2.5 \text{ m s}^{-1}$	Avg. vapor flux ( $\text{kg m}^{-2} \text{ s}^{-1}$ )	Avg. frozen flux ( $\text{kg m}^{-2} \text{ s}^{-1}$ )	Avg. ice flux ( $\text{kg m}^{-2} \text{ s}^{-1}$ )	Avg. snow flux ( $\text{kg m}^{-2} \text{ s}^{-1}$ )	Avg. graupel flux ( $\text{kg m}^{-2} \text{ s}^{-1}$ )
NICAM	1	5.4 %	0.010 %	$7.1 \times 10^{-10}$	$1.6 \times 10^{-6}$	$3.2 \times 10^{-7}$	$5.4 \times 10^{-7}$	$7.6 \times 10^{-7}$
	2	66.4 %	0.022 %	$4.9 \times 10^{-9}$	$5.5 \times 10^{-8}$	$3.9 \times 10^{-8}$	$1.5 \times 10^{-8}$	$4.5 \times 10^{-11}$
	3	28.1 %	0.003 %	$3.2 \times 10^{-9}$	$5.0 \times 10^{-10}$	$3.9 \times 10^{-10}$	$1.1 \times 10^{-10}$	$2.2 \times 10^{-16}$
FV3	1	4.8 %	0.039 %	$7.3 \times 10^{-8}$		$1.8 \times 10^{-6}$		
	2	29.2 %	0.039 %	$1.4 \times 10^{-8}$		$6.6 \times 10^{-8}$		
	3	37.2 %	0.007 %	$1.1 \times 10^{-8}$		$3.1 \times 10^{-9}$		
ICON	1	2.8 %	0.001 %	$1.4 \times 10^{-9}$		$1.1 \times 10^{-7}$		
	2	32.1 %	0.009 %	$-3.9 \times 10^{-9}$		$9.5 \times 10^{-9}$		
	3	33.5 %	0.005 %	$4.8 \times 10^{-9}$		$4.7 \times 10^{-10}$		
SAM	1	3.7 %	0.213 %	$9.9 \times 10^{-9}$		$2.3 \times 10^{-6}$		
	2	39.5 %	0.055 %	$5.8 \times 10^{-9}$		$1.9 \times 10^{-7}$		
	3	37.0 %	0.008 %	$2.8 \times 10^{-8}$		$1.5 \times 10^{-8}$		

*Note.* Same as Table 2 in the paper, but for the TWP.